COHERENT SCATTERING OF HELICAL EDGE ELECTRONS FROM NUCLEAR SPINS

by
DENİZ BOZ

Submitted to the Graduate School of Engineering and Natural Sciences
in partial fulfillment of the requirements for the degree of
Master of Science

Sabancı University
January 2019

COHERENT SCATTERING OF HELICAL EDGE ELECTRONS FROM NUCLEAR SPINS

APPROVED BY

Assoc. Prof. İnanç Adagideli
(Thesis Supervisor) .....

Prof. Zafer Gedik .....

Assoc. Prof. Levent Subaşı .....

DATE OF APPROVAL 07/01/2019

ABSTRACT

COHERENT SCATTERING OF HELICAL EDGE ELECTRONS FROM NUCLEAR SPINS

Deniz Boz

Master Thesis, January 2019

Thesis Supervisor: Assoc. Prof. İnanç Adagideli

Keywords: Mesoscopic and nanoscale systems, topological insulators, edge states, magnetic impurities, hyperfine interaction, spin polarization, spin current

Topological insulators (TIs) are symmetry-protected states of matter characterized by a topological index, featuring gapless edge or surface states that are topologically protected, hence robust to weak disorder as long as the relevant anti-unitary symmetry is preserved. In this thesis, we focus on a particular TI, namely the quantum spin Hall insulator, where the relevant symmetry is the time-reversal (TR) symmetry. However, most topological insulators contain nuclear spins, which interact with the helical edge states via hyperfine coupling, breaking the TR symmetry and thus destroying the topological protection of the edge states. We perform numerical simulations to calculate the hyperfine-enabled backscattering probabilities of the helical edge electrons for edges containing up to 10 nuclear spins. We presented the plots of total reflection probabilities for a range of single-nucleus reflection amplitudes and discuss how our results apply to dynamic nuclear polarization. We also propose a universal extremum of the total reflection probability curves, independent of the system size, and expose which particular arrangements of nuclear spins cause the universal extremum.

ÖZET

SARMAL KENAR ELEKTRONLARININ NÜKLEER SPİNLERDEN EŞEVRELİ SAÇILIMI

Deniz Boz

Yüksek Lisans Tezi, Ocak 2019

Tez Danışmanı: Doç. Dr. İnanç Adagideli

Anahtar kelimeler: Mezo ve nanoölçekli sistemler, topolojik yalıtkanlar, kenar durumları, manyetik safsızlıklar, aşırı ince etkileşim, spin kutuplaşması, spin akımı

Topolojik yalıtkanlar maddenin topolojik bir indis tarafından karakterize edilmiş, simetri korunumlu, topolojik olarak korunan ve bu sebeple ilgili anti-üniter simetri korunduğu sürece zayıf safsızlıklara ve bant aralığı oluşumuna karşı dayanıklı kenar ya da yüzey durumları içeren halleridir. Bu tezde, ilgili simetrinin zaman tersinme simetrisi olduğu, kuantum spin Hall yalıtkanı olarak bilinen bir topolojik yalıtkana odaklandık. Öte yandan, birçok topolojik yalıtkan aşırı ince etkileşim suretiyle sarmal kenar elektronlarıyla etkileşen ve bu yolla zaman tersinme simetrisini kırarak topolojik korunumu yok eden nükleer spinler içerir. Sayısal benzetim kullanarak en fazla 10 nükleer spin içeren kenarlar için sarmal kenar elektronlarının aşırı ince etkileşim kaynaklı geri saçılım olasılıklarını hesapladık. Belirli bir tek-çekirdek yansıma genliği aralığı için tam yansıma olasılığı grafiklerini sunduk ve sonuçlarımızın dinamik nükleer kutuplaşmaya nasıl uygulanabileceğini tartıştık. Ayrıca sistem boyutundan bağımsız bir evrensel uçdeğer (ekstremum) önerdik ve hangi nükleer spin dizilimlerinin bu evrensel uçdeğere sebep olduğunu bulduk.

ACKNOWLEDGEMENTS

First off, I would like to thank my advisor, Assoc. Prof. İnanç Adagideli, for his guidance, patience and encouragement throughout my master studies. I would like to acknowledge him for providing a fertile academic environment and giving me the oppurtunity to work with him in the first place; his high standarts for research helped me to constantly challenge and improve myself as a student of science.

I would also like to thank the fellow members of our research group, mostly to three people, namely Barış Pekerten, A. Mert Bozkurt and Ali Asgharpour. Evidently, one of the most fortunate things to have as a graduate student is a group of peers that are one or two steps ahead of you in the journey. They were always there to patiently address my hundreds of questions. Completing this thesis would not be possible without them.

Finally, I would like to express my deepest gratitude to my family, especially to my mother, for always being there and supporting me no matter what, in this somewhat convoluted journey that is called life.

Contents

List of Figures and Tables

Chapter 1

INTRODUCTION

In this thesis, we study the backscattering of helical edge electrons from nuclear spins. This process is due to the hyperfine (HF) coupling of the electron spins to that of the nuclei in 1D edge channels of 2D topological insulators. Specifically, we calculate the probability of total reflection for non-interacting electrons scattering from a region of nuclear spins.

This thesis is organized as follows. In Chapter 2, we begin by giving an introduction to quantum Hall effect (QHE), which is historically the first example of a long list of topologically nontrivial materials. We next provide a selected survey on topological insulators with focus on subjects that are particularly relevant to this thesis. We also provide an expression for the edge state wavefunctions of the Bernevig-Hughes-Zhang (BHZ) model. We conclude the chapter by providing a brief description of the HF interaction in semiconductors as well as a description of transport formalism that we use in this thesis.

In Chapter 3, we start with the Fermi point contact (FPC) interaction between the electron and the nuclear spin, which is the dominant term in HF coupling for 1D edge channels. We solve for the eigenstates of the Hamiltonian that governs the system, and introduce the probability amplitudes for single-nucleus scattering. We next define an anti-unitary symmetry which we refer to as the global time-reversal (GTR) symmetry, which is preserved even though the conventional time-reversal (TR) symmetry is broken. We then examine the behavior of helical edge states under the action of the GTR symmetry. By comparing the resulting wavefunctions at the ends of interaction region to the original eigenstates, we find a useful relation between reflection and transition amplitudes which we exploit in our numerical calculations.

In Chapter 4, we present a straightforward formula that gives the overlap between the initial and final states of the overall system. We then depict a so-called probability-amplitude tree and explain how our program executes the formula and calculates the probability of total reflection for scattered electrons. We report our results by providing the plots of total reflection probability for edge channels containing up to 10 nuclear spins, as

a function of the single-nucleus reflection amplitudes, $|r|^2$. We find that all the plots share a common extremum at a specific value of $|r|^2$, suggesting a universality at this point, independent from the system size. We also find that initial nuclear spin configurations with down spins piled up mostly at the further side of interaction region contribute the most to this universal extremum. We conclude this chapter by considering the possible applications of our findings, as well as future directions for our work.

Finally, in Chapter 5, we summarize our results and conclusions.

Chapter 2

OVERVIEW

In this chapter, we provide an overview of the 2D topological insulators (TIs) that are relevant for the rest of this thesis. We first introduce the quantum Hall effect (QHE) [1] starting from the basics in Section 2.1. We then review the type of time-reversal (TR) symmetry protected TI that we focus in this thesis, namely the quantum spin Hall (QSH) system, introduce a model to solve for the edge states, and present the idea of topological protection in Section 2.2. Finally, we outline the hyperfine (HF) interaction, and introduce scattering matrix in simple one-dimensional (1D) systems, in Sections 2.3 and 2.4.

2.1. Quantum Hall Effect

If we confine a number of electrons in a two-dimensional slab, let them move under the effect of an electric field along one direction, and apply an external magnetic field perpendicular to the slab, we would observe a potential difference between the edges of the slab *perpendicular to* the electric field. This potential difference is called the *Hall* voltage. We discuss classical Hall effect in further detail in Section, 2.1.1. The Hall conductance is defined as the ratio of the current in the direction of the electric field to the Hall voltage. If we apply a very strong external magnetic field, the Hall conductance is observed to have quantized values:

$$\sigma_{xy} = \frac{e^2}{h}\nu, \tag{2.1}$$

where $-e$ is the charge of the electron, h is the Planck's constant, and ν is the multiplicative factor. This is called the quantum Hall effect (QHE) [1]. At first, the factor ν was found to be integer valued to a great precision [2, 3]. This was an example of a quantum effect seen in a macroscopic scale. What was even more surprising was that this property appeared to be not affected by how dirty the system is to a great extent [4]. We discuss QHE in further detail in Section 2.1.2.

Later, it was discovered that the factor ν can also take rational values, but only cer-

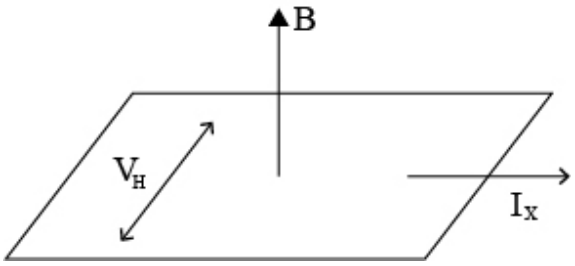

Figure 2.1: The classical Hall effect. An external magnetic field in z-direction is applied to a current flowing in x-direction, leading an induced voltage between the edges of the sample.

tain ones. Well known examples are $\nu = 1/3$ and $2/5$, among many that have been observed [5]. It turned out that this time, interactions between electrons are in play. This fractional version of quantum hall effect is out of scope of this thesis, thereby will not be reviewed in further detail. The reader may check Asboth *et al.* [6] and references therein for a detailed discussion of the topic. We review only integer quantum Hall effect.

Because of its remarkable behavior, the Quantum Hall Effect remains as an exciting medium of new ideas for promising technologies and novel phenomena in solid state physcics. It is especially proven to be of importance in the way that it shows how topology comes into play in quantum mechanics, paving the way for topological insulators.

2.1.1. Classical Hall Effect

The Hall effect [7] arguably is one of the most famous phenomena in physics. Consider the case of electrons confined to move in the plane perpendicular to the z-direction, while a uniform current is applied in the longitudinal direction, which we choose to be x. A simple setup can be seen in Figure 2.1. If a constant magnetic field **B** is applied in the z-direction, the magnetic field induces a voltage in the y-direction. This voltage, V_H, is called the *Hall voltage* and this phenomenon is referred to as the *Hall effect*.

The Hall effect is due to the motion of charged particles in an external magnetic field. The equation of motion for such a particle is given as

$$m\frac{d\mathbf{v}}{dt} = -e\mathbf{v} \times \mathbf{B}, \tag{2.2}$$

where m is the mass and $-e$ is the charge of the particle. If we have a magnetic field pointing in the z-direction, $B\hat{z}$, the velocity of the particle is $\mathbf{v} = (\dot{x}, \dot{y}, 0)$, as long as the particle is restricted to move in the (x, y)-plane. Consequently, the equations of motion are given as coupled differential equations

$$m\ddot{x} = -eB\dot{y} \quad \text{and} \quad m\ddot{y} = eB\dot{x}. \tag{2.3}$$

The general solution to the equations of motion is

$$x(t) = x_0 - R\sin(\omega_c t + \phi) \quad \text{and} \quad y(t) = y_0 + R\sin(\omega_c t + \phi), \tag{2.4}$$

where R is the radius of circle, ϕ is the arbitrary phase, and ω_c is the constant frequency of the circular motion of the particle, given as

$$\omega_c = \frac{eB}{m}, \tag{2.5}$$

which is called the *cyclotron frequency*. We know that for circular motion, the linear and angular velocities are related by $v = \omega r$, in scalar quantities. The cyclotron radius will be $r_c = \dfrac{v}{\omega_c} = \dfrac{mv}{eB}$, and the angular momentum of the electron is given as $L = mvr_c = eBr_c^2$. Since the angular momentum values must be quantized as $L = n\hbar$, the radius admits only discrete values, given as $r_n = \sqrt{n} l_B$, where $l_B = \dfrac{\hbar}{eB}$ is called the *magnetic length*.

If we add two more components to this system, namely an electric field, **E**, and a friction term, which represents the effect of electron scattering by the potential impurities, we get a more complex, yet more informative picture. The new equation of motion is given by

$$m\frac{d\mathbf{v}}{dt} = -e\mathbf{E} - e\mathbf{v} \times \mathbf{B} - \frac{m\mathbf{v}}{\tau}, \tag{2.6}$$

where the last term is due to friction, and τ is the average time between the collisions, sometimes called as *mean free time* or *momentum relaxation time*. Equation 2.6 is the simplest model in transport literature, and it views electrons as classical particles without any quantum effects. The model described by Equation 2.6 is called the *Drude model* [8].

To obtain the conductivity (and resistivity) of the system, we are interested in solutions where the system is at equilibrium, which entails $\dfrac{d\mathbf{v}}{dt} = 0$. Equation 2.6 then becomes

$$\mathbf{v} + \frac{e\tau}{m}\mathbf{v} \times \mathbf{B} = -\frac{e\tau}{m}\mathbf{E}. \tag{2.7}$$

We can write the current density as $\mathbf{J} = -ne\mathbf{v}$, where n is the electron density, then Equation 2.7 takes the form

$$\begin{pmatrix} 1 & \omega_c\tau \\ -\omega_c\tau & 1 \end{pmatrix} \mathbf{J} = \frac{e^2 n\tau}{m}\mathbf{E}. \tag{2.8}$$

If we invert this matrix and absorb the multiplicative factors, we get the equation

$$\mathbf{J} = \bar{\bar{\sigma}}\mathbf{E}. \tag{2.9}$$

This is the famous *Ohm's law*, relating the applied electric field to the resulting current.

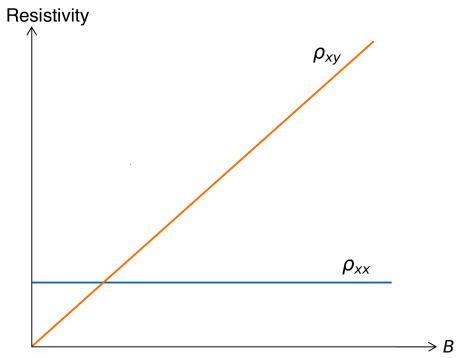

Figure 2.2: The classical expectation of resistivities in x and y-direction, as a function of magnitude of an increasing external magnetic field.

The proportionality factor $\bar{\bar{\sigma}}$ is called the *conductivity* of the system, and is given by

$$\bar{\bar{\sigma}} = \frac{\bar{\bar{\sigma}}_0}{1+\omega_c^2\tau^2}\begin{pmatrix} 1 & -\omega_c\tau \\ \omega_c\tau & 1 \end{pmatrix}. \tag{2.10}$$

Note that when there is no magnetic field, the electric field will accelerate the charges and would result a current in the direction of the electric field. Therefore, in the absence of a magnetic field, $\bar{\bar{\sigma}}$ will be proportional to the identity matrix, given by

$$\bar{\bar{\sigma}}_0 = \frac{e^2 n\tau}{m}\begin{pmatrix} 1 & 0 \\ 0 & 1 \end{pmatrix}. \tag{2.11}$$

The off-diagonal terms of the matrix in Equation 2.10 captures the Hall effect. The off-diagnoal terms dictate that a current in x-direction entails that the electric field has a component in y-direction. It's this component of the electric field that is responsible for the Hall voltage, V_H. The resistivity is written as

$$\bar{\bar{\rho}} = \bar{\bar{\sigma}}^{-1} = \frac{m}{e^2 n\tau}\begin{pmatrix} 1 & \omega_c\tau \\ -\omega_c\tau & 1 \end{pmatrix}. \tag{2.12}$$

Notice that when we substitute Equation 2.5 for ω_c, we see that $\rho_{xy} = \dfrac{B}{ne}$, which is independent of mean free time τ, and thereby independent from how dirty the material is. On the other hand, the resistivity in the x-direction depends on mean free time, as it is given by $\rho_{xx} = \dfrac{m}{e^2 n\tau}$. Note that $\rho_{xx} \to 0$ as $\tau \to \infty$, which is expected from a conductor which is virtually free of impurities. If we are to plot ρ_{xx} and ρ_{xy} with respect to the magnetic field, the expected behavior would be as shown in Figure 2.2.

2.1.2. Integer Quantum Hall Effect

The integer quantum Hall effect was first discovered experimentally, and then conceived theoretically. The first set of experiments demonstrating the effect was conducted by von Klitzing in 1980 [1]. He found that, as we increase the strength of the magnetic field, the Hall resistivity and the longitudinal resistivity show different behavior than classical expectation (recall Figure 2.2). The Hall resistivity, ρ_{xy}, remains constant for a range of magnetic field, then makes a jump, and then remains constant again for another range, exhibiting "plateaux". The longitudinal resistivity, ρ_{xx}, on the other hand, exhibits peaks where the ρ_{xy} jumps occur and vanish otherwise.

On these plateaux, the Hall resistivity takes the values

$$\rho_{xy} = \frac{h}{e^2\nu}, \tag{2.13}$$

where ν is measured to be an integer. The quantity $\dfrac{e^2}{h}$ is called the *conductance quantum*, where $-e$ is the charge of an electron and h is the Planck's constant.

We substitute Equation 2.5 into Equation 2.12 and get $\rho_{xy} = \dfrac{B}{ne}$. Using this expression, we note that at the center of each plateau, the magnetic field takes the value

$$B = \frac{hn}{\nu e} = \frac{n}{\nu}\Phi_0, \tag{2.14}$$

where n is the electron density and $\Phi_0 = \dfrac{h}{e}$ is called the *magnetic flux quantum*. Now we write conductivity and resistivity from Equations 2.10 and 2.12 in the matrix form:

$$\sigma = \begin{pmatrix} \sigma_{xx} & \sigma_{xy} \\ -\sigma_{xy} & \sigma_{yy} \end{pmatrix} \quad \text{and} \quad \rho = \begin{pmatrix} \rho_{xx} & \rho_{xy} \\ -\rho_{xy} & \rho_{yy} \end{pmatrix}, \tag{2.15}$$

which in turn give components

$$\sigma_{xx} = \frac{\rho_{xx}}{\rho_{xx}^2 + \rho_{xy}^2} \quad \text{and} \quad \sigma_{xy} = \frac{-\rho_{xy}}{\rho_{xx}^2 + \rho_{xy}^2}. \tag{2.16}$$

Remember that ρ_{xx} vanishes as ρ_{xy} remains constant as a plateau. Normally, we say that a system with $\rho_{xx} = 0$ is virtually a perfect conductor. If $\rho_{xy} = 0$, we obtain the conventional relation between conductivity and resistivity: one is the inverse of the other. However, if $\rho_{xy} \neq 0$, something very peculiar is going on:

$$\rho_{xx} = 0 \quad \Rightarrow \quad \sigma_{xx} = 0.$$

It seems as if the system is a perfect conductor and a perfect insulator at the same time. In fact, the discrepancy arises because of how we define conductance and resistance in

physics. The fact that $\rho_{xx} = 0$ and $\sigma_{xx} = 0$ at the same time simply shows that the current flows in the direction perpendicular to the electric field.

2.1.3. Landau Levels

Before we continue, it is of use to review some basics. Lagrangian of a classical particle with mass m and charge $-e$ in the presence of an external magnetic field $\mathbf{B} = \nabla \times \mathbf{A}$ is

$$L = \frac{1}{2}m\dot{\mathbf{x}}^2 - e\dot{\mathbf{x}} \cdot \mathbf{A}. \tag{2.17}$$

Under the gauge transformation $\mathbf{A} \to \mathbf{A} + \nabla\alpha$, the Lagrangian changes as $L \to L - e\dot{\alpha}$. Since the Lagrangian is defined to within an additive total time derivative of any function, the equations of motion will remain unchanged. The canonical momentum of this Lagrangian is $\mathbf{p} = \dfrac{\partial L}{\partial \dot{\mathbf{x}}} = m\dot{\mathbf{x}} - e\mathbf{A}$. Accordingly, the Hamiltonian, which is $H = \dot{\mathbf{x}} \cdot \mathbf{p} - L$, takes the form

$$H = \frac{1}{2m}(\mathbf{p} + e\mathbf{A})^2. \tag{2.18}$$

Since our magnetic field B is pointing in the z-direction, we choose $\mathbf{A} = yB\hat{\mathbf{x}}$, also known as the *Landau gauge*. The magnetic field is invariant under both translation and rotation. On the other hand, since it does not depend on x, the vector potential $\mathbf{A}$ does not break the translational symmetry in x-direction, however, it breaks in y-direction. Hence $[H, p_x] = 0$, leading to $\hat{p}_x \to p_x = \hbar k$, with $k \in \mathbb{R}$. Now the Hamiltonian in Equation 2.18 becomes

$$H = \frac{1}{2m}(p_y^2 + (\hbar k + eBy)^2), \tag{2.19}$$

with eigenvalues giving the Landau levels. Note that for a given chemical potential, when precisely n Landau levels are filled, integers n and ν in Equation 2.1 are actually the same. It is also possible to introduce raising and lowering operators and write the Hamiltonian in terms of these operators. If this Hamiltonian acts on the eigenstates starting from the ground state, the energy of the nth eigenstate is determined as

$$E_n = \hbar\omega_c(n + \frac{1}{2}), \tag{2.20}$$

where ω_c is the cyclotron frequency. An explicit calculation can be found in any quantum mechanics textbook, whereas further details in Jain [9]. These energy levels are called the *Landau levels*. Note that they look very different from the energy spectrum of a particle without an external magnetic field applied, for they are equally spaced with gaps that are proportional to the magnitude of the magnetic field, B, as can be seen in Figure 2.3.

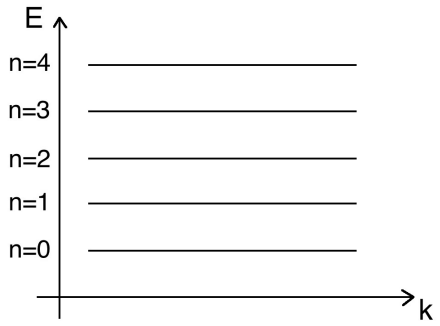

Figure 2.3: First few Landau levels.

2.1.4. Edge Modes

As is well known, classical charged particles move in circles in the presence of an external magnetic field. If the magnetic field is uniform and constant, all motion will be in one direction, depending on the direction of **B**. At the edges of our sample, the circular orbits will be blocked by the boundaries of the sample. Figure 2.4 depicts a cartoon picture version of classical circular orbits blocked by the boundary of the sample, resulting in a motion looking like skipping half circles along the edge. The real picture is more complicated; if this is quantized, we get the edge modes [10]. These sates are called the *chiral edge states*, and since the particles moving in opposite directions on the opposite sides of the sample, hence they have opposite *chirality*. The chirality of the edge states depend on the orientation of the magnetic field. Also note that in the absence of an electric field, the net current becomes zero. The edges of the sample can be modeled by an infinite potential, $V(y)$, that steeply rises at the edges. Choosing the Landau gauge and working in a sample that is finite in the y-direction, the Hamiltonian is

$$H = \frac{1}{2m}(p_y^2 + (p_x + eBy)^2) + V(y). \tag{2.21}$$

Since the potential is constant in the bulk, where the Landau levels are flat, as shown in Figure 2.3, it can be taken as $V(y) = 0$. Here, the wavefunctions are Gaussian with width l_B. These are the states with cyclotron orbits that are shown in Figure 2.4. As we get closer to the edges, however, the energies of the states are easily affected by the confining potential. Using the Hamiltonian given in Equation 2.21 and Hamilton's equation $dx/dt = \partial H/\partial p_x$, we get $p_x = mv_x - eBy$. Using the Hamilton's equation $dp_y/dt = -\partial H/\partial y$, we also get

$$-\frac{dp_y}{dt} = \frac{eB}{m}(p_x + eBy) + \frac{\partial V}{\partial y}.$$

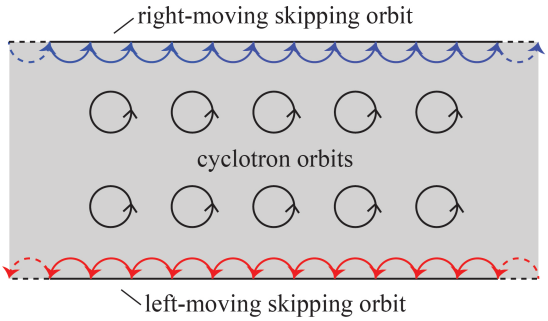

Figure 2.4: A simplified picture of uni-directional chiral edge modes in a 2D sample.

Substituting $p_x = mv_x - eBy$ into the above equation, we obtain

$$-\frac{dp_y}{dt} = eBv_x + \frac{\partial V}{\partial y}.$$

Since the force of the electric field due to the Hall voltage cancels the Lorentz force in the y-direction at equilibrium, we have $F_y = dp_y/dt = 0$. Therefore we get

$$v_x = -\frac{1}{eB}\frac{\partial V}{\partial y}. \tag{2.22}$$

Because of the derivative term, the states at the opposite sides of the sample have opposite velocities, as shown in Fig 2.4. It can also be viewed as the wavefunctions with positive and negative k are propagating at the opposite edges. In other words, the quantum Hall system is a gapped system, but the gap is closed at the edges of the sample.

This is a manifestation of the so called bulk-edge correspondance, for the chiral edge states could not be realized without the existence of the gapped states in the bulk of the sample. Although they exist in one dimension, the chiral edge states cannot exist in other one-dimensional systems, such as a quantum wire. Also note that the presence of the edge states is not affected by the shape or size of the sample, or the number of impurities.

2.2. Topological Insulators

The quantum Hall (QH) state was the first topologically nontrivial state of matter that was discovered [1]. The two-dimensional sample demonstrated an insulating bulk and conducting edges without dissipation, giving rise to the quantized Hall effect, as we have shown in the preceding section. It lead to the definition of the *topological invariant* by Thouless [3] and by Laughlin [11], which could take values of integer multiples of e^2/h for the QH system.

In mathematics, the subfield of topology classifies different objects by their geometrical properties and spatial relations that are preserved under continuous deformations. The most famous example is that of a donut and a coffee cup. They belong to the same

topological class since both have a single hole; we can mold one from another without creating a hole, tearing, or gluing.

By the same token, any transformation on the Hamiltonian of a many particle system that does not close the gap can be considered as continuous, where the topological invariant remains unchanged [12]. On the other hand, a transformation that closes the band gap might change the topological invariant. If the topological invariant changes, the transition is called a *topological phase transition*. Topological classes of different band structures are differentiated by the *Chern invariant*, for which the equation is provided in Section 2.2.5. Thouless *et al.* also introduced the TKNN invariant (after Thouless, Kohomoto, Nightingale and den Nijs), which relates the quantized Hall conductivity in Equation 2.1 to the Chern invariant. A quantized physical quantity can be expressed in terms of an invariant integral over a coordinate, such as the momentum space [3, 13]. These physical quantities, including the quantized Hall conductance for the QH state, uniquely define the quantum state of matter, thus serve as the topological order parameter. Even further advance was the development of the Topological Field Theory [14], which is not relevant for our work and therefore will not be covered.

2.2.1. Quantum Spin Hall Effect

About two decades after the discovery of the QH effect, a new class of topological state, namely the quantum spin Hall (QSH) effect, was proposed [15]. Like the QH state, QSH state has an energy gap in the bulk, and gapless edge states at the boundaries, which are robust against the impurities and geometric irregularities in the sample [16]. Unlike the QH state, however, the QSH state can be obtained without applying a magnetic field and the TR symmetry is intact.

In a quasi-one-dimensional conductor, random scattering causes the forward and backward moving states to mix and gives rise to electrical resistance. In the QH state, however, these states are separated into opposite edges of the sample. Hence a local perturbation cannot cause back-scattering. As a result, the chiral edge states are robust against the impurities; they perpetually move in the same direction despite the impurities, as shown in Figure 2.5 (a).

It turns out that it is possible to obtain a similar state without applying a magnetic field. Up to now, the spin degree of freedom in QH system is not discussed. In a real 1D system, both spin-up and spin-down electrons move in both directions, producing four channels in total. Separation of these states is possible with the help of spin-orbit (SO) coupling, as first predicted in 2005 [17] and in 2006 [16]. Hence one may have a spin-up ($\nu = 1$) QHE and spin-down ($\nu = -1$) QHE, which we call the QSHE. In

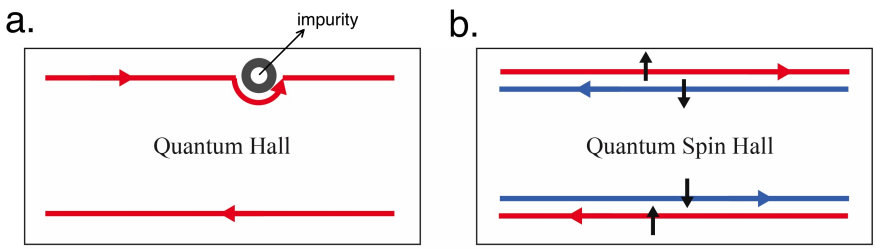

Figure 2.5: (a) Spinless right-moving and left-moving electrons are separated in opposite edges of the system, whereas (b) QSH system contains an oppositely moving pair of spin-up and spin-down electrons in opposite edges.

the QSH state, up-spin forward movers and down-spin backward movers are propagating on the upper edge, while the complete opposite propagating on the bottom, as shown in Figure 2.5 (b). Forward movers and backward movers on a given edge are Kramers pairs, meaning these states are doubly degenerate. Because of this spin-momentum locked nature, the edge states are sometimes referred as the *helical edge states* [18]. For an edge electron, there are no states availabe with same the spin and opposite momentum on the edge it propagates, therefore only forward scattering is allowed. This renders helical edge states significant robustness. However, if there were two Kramers pairs on a given edge, in a way that oppositely moving electrons have the same spin, an electron could reflect to oppositely moving channel preserving its spin, resulting in reflected waves that interfere randomly, hence dissipation would be inevitable. Indeed, Kane and Mele showed that in order to have a stable QSH system, a given edge of the sample must contain an odd number of oppositely moving Kramers pairs [17, 19]. This topological feature of QSH state is represented by the $\mathbb{Z}_2$ topological invariant; systems with an even number of Kramers pairs on a given edge is classified as topologically trivial, while the ones with an odd number of Kramers pairs as nontrivial. For further detail, see Kane and Mele [19].

In the case of a magnetic impurity or a nuclear spin, its hyperfine coupling to the helical edge states breaks the TR symmetry and causes backscattering, which is the subject of this thesis.

2.2.2. Spin-Orbit Interaction

Before providing the BHZ model, we first briefly describe the spin-orbit (SO) interaction, which is a relativistic effect that plays an essential role in the QSH phenomenon. Consider the simplest hydrogen atom with only a single proton and a single electron. In the frame of the electron, the proton is orbiting around it. As a circling positive charge, the proton's "current" gives rise to a magnetic field, $\mathbf{B}$, exerting a torque on the electron, coupling with its magnetic moment, $\boldsymbol{\mu}$. Hence the Hamiltonian term for the interaction is given by

$H_{SO} = -\boldsymbol{\mu} \cdot \mathbf{B}$. Magnetic moment of the electron is proportional to its spin, **S**, and the magnetic field applied by the orbiting proton is proportional to its angular momentum, **L**, making the Hamiltonian take the form of **S**·**L**, with some multiplicative constants [20]:

$$H_{SO} = \frac{1}{m_e^2 c^2} \frac{1}{r} \frac{dV_c}{dr} (\mathbf{S} \cdot \mathbf{L}), \tag{2.23}$$

where m_e is the electron mass, c is the speed of light and V_c is the Coulomb potential.

Although present in all materials, SO coupling is stronger in heavier elements due to larger spins. In many semiconductors, the conduction band consists of electrons from s orbitals, while the valence band does from p orbitals. In some specific, heavier elements, however, band inversion between s and p orbitals occurs, due to strong SO coupling [21].

2.2.3. Bernevig-Hughes-Zhang (BHZ) Model

In 2006, it was predicted that QSH state can be realized in HgTe quantum wells [15]. The wells are formed by sandwiching HgTe between two layers of CdTe. The lattice constant of CdTe is close to HgTe, but the effect of SO coupling is significantly smaller compared to HgTe. Since increasing HgTe layer thickness consequently increases the SO coupling strength, researchers predicted a topological phase transition as a function of the thickness of the quantum well, d_{QW}. Since CdTe has a much weaker SO coupling, when the well is thin, CdTe has dominance and the bands have the ordering of an ordinary insulator. When the well is wide, i.e., HgTe layer is thicker, HgTe gets dominant and the order of the bands is inverted, as shown in Figure 2.6. The inversion of the bands leads to a topologically nontrivial state. The critical thickness, d_c, where the band inversion occurs, is predicted to be about 6.5nm [15]. The experimental confirmation came shortly after [22, 23].

The effective Hamiltonian of the BHZ model is given by:

$$H_{\text{eff}}(\mathbf{k}) = \epsilon(k)\mathbf{1} + \begin{pmatrix} M(k) & A(k_x + ik_y) & 0 & 0 \\ A(k_x - ik_y) & -M(k) & 0 & 0 \\ 0 & 0 & M(k) & -A(k_x - ik_y) \\ 0 & 0 & -A(k_x + ik_y) & -M(k) \end{pmatrix},$$

$$\epsilon(\mathbf{k}) = C - D(k_x^2 + k_y^2), \quad M(\mathbf{k}) = M - B(k_x^2 + k_y^2), \tag{2.24}$$

where σ_i are the Pauli matrices. Written in a basis given by electron and heavy hole bands, $|E\uparrow\rangle$, $|H\uparrow\rangle$, $|E\downarrow\rangle$ and $|H\downarrow\rangle$, respectively, this Hamiltonian is obtained by expanding the interactions between the the highest valence band and the lowest conduction band in the $\mathbf{k} \cdot \mathbf{p}$ approximation [24]. The parameter A describes the coupling of the bands to the

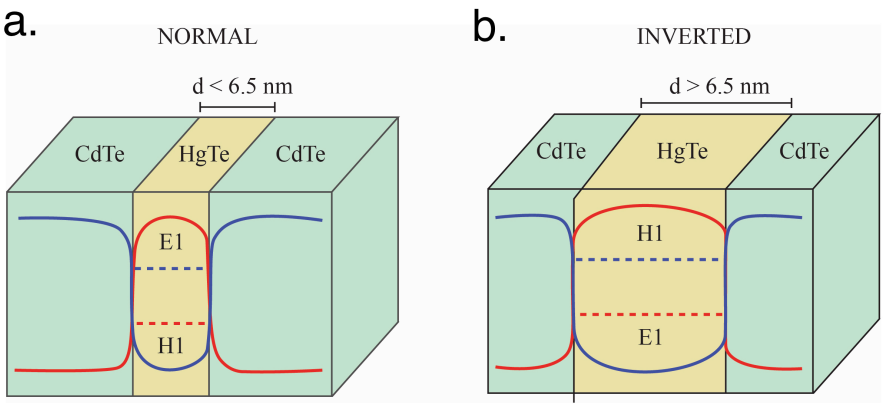

Figure 2.6: The band structure of the HgTe quantum wells depending on the thickness of the well. Blue curves denote the potential energy for conduction electrons, and the red curves denote those of the holes in the valence band. (a) When the thickness is less than the critical value, $d < d_c$, the lowest conduction band, E1, is above the the highest valence band, H1, in energy, as usual. But (b) when the thickness is larger than the critical value, $d > d_c$, the bands are inverted [25].

lowest order, B describes the curvature of the bands, and M is the mass parameter, which changes sign at $d = d_c$, where two bands become degenerate. The energy gap between the bands is $2M$. Accordingly, the energy spectrum of the bulk is given by

$$E_{\pm} = \epsilon(k) \pm \sqrt{A^2(k_x^2 + k_y^2) + M^2(k)}. \tag{2.25}$$

The BHZ model provides us a framework in which we can explicitly solve the helical edge states, as will be carried out in the next subsection.

2.2.4. Helical Edge States

In order to obtain obtain the expressions for the helical edge states, we solve the BHZ model by following the steps of Qi and Zhang [25]. We consider the Hamiltonian given in Equation 2.24, defined on the half-space $x > 0$ in the (x, y)-plane. We rewrite the Hamiltonian as $H = H_0 + H_1$, where

$$\begin{aligned} H_0 &= \epsilon(k_x) + \begin{pmatrix} M(k_x) & A(k_x) & 0 & 0 \\ A(k_x) & -M(k_x) & 0 & 0 \\ 0 & 0 & M(k_x) & -A(k_x) \\ 0 & 0 & -A(k_x) & -M(k_x) \end{pmatrix}, \\ H_1 &= -Dk_y^2 + \begin{pmatrix} -Bk_y^2 & iA(k_y) & 0 & 0 \\ -iA(k_y) & Bk_y^2 & 0 & 0 \\ 0 & 0 & -Bk_y^2 & iA(k_y) \\ 0 & 0 & -iA(k_y) & Bk_y^2 \end{pmatrix}, \end{aligned} \tag{2.26}$$

where $\epsilon(k_x) = C - Dk_x^2$ and $M(k_x) = M - Bk_x^2$. Since the system has an open boundary with the half space, we replace k_x with the operator $-i\partial_x$. For $k_y = 0$, which is a "good" quantum number for translation symmetry is preserved along the y-direction, we get $H_1 = 0$. The Schrödinger equation has the form

$$H_0(k_x \to -i\partial_x)\Psi(x) = E\Psi(x). \tag{2.27}$$

Since H_0 is block-diagonal, the eigenstates are written as

$$\Psi_\uparrow(x) = \begin{pmatrix} \psi_0 \\ \mathbf{0} \end{pmatrix}, \quad \Psi_\downarrow(x) = \begin{pmatrix} \mathbf{0} \\ \psi_0 \end{pmatrix}, \tag{2.28}$$

where $\mathbf{0}$ is the 2×1 zero vector, and the localized wavefunction $\psi_0(x)$ at the edge satisfies the Schrödinger equation

$$\left[\epsilon(-i\partial_x) + \begin{pmatrix} M(-i\partial_x) & -iA_1\partial_x \\ -iA_1\partial_x & -M(-i\partial_x) \end{pmatrix}\right]\psi_0(x) = E\psi_0(x). \tag{2.29}$$

If we ignore ϵ, this wave equation would have a particle-hole symmetry, leading to an edge state with zero energy. With the ansatz $\psi_0 = \phi e^{\lambda x}$, the real part of the solution near $\mathbf{k} = 0$ is

$$\psi_0(x) = \begin{cases} N_\uparrow(e^{\lambda_1 x} - e^{\lambda_2 x})\phi_-, & A/B < 0 \\ N_\downarrow(e^{-\lambda_1 x} - e^{-\lambda_2 x})\phi_+, & A/B > 0 \end{cases} \tag{2.30}$$

$$\lambda_{1,2} = \frac{1}{2B}(A \pm \sqrt{A^2 - 4MB}),$$

where $N_{\uparrow,\downarrow}$ are the normalization constants, and $\phi_\pm$ are spinors defined by $\sigma_y\phi_\pm = \pm\phi_\pm$. Projecting the bulk Hamiltonian onto these edge states, we obtain the effective edge Hamiltonian as

$$H_{edge} = Ak_y\sigma_z. \tag{2.31}$$

These edge states have opposite spin and momentum and are the previously mentioned counter-propagating states in Section 2.2.1. The analytical calculation can be confirmed by numerically diagonalizing the Hamiltonian on a finite-width strip [26]. Figure 2.7 shows the dispersion relation of the system below and above the critical thickness, d_c, respectively. Below d_c, the system demonstrates the spectrum of an ordinary insulator, where the conduction and the valence bands are separated by an energy gap. Above d_c, the bands are connected by the edge states, as shown in Figure 2.7 (b).

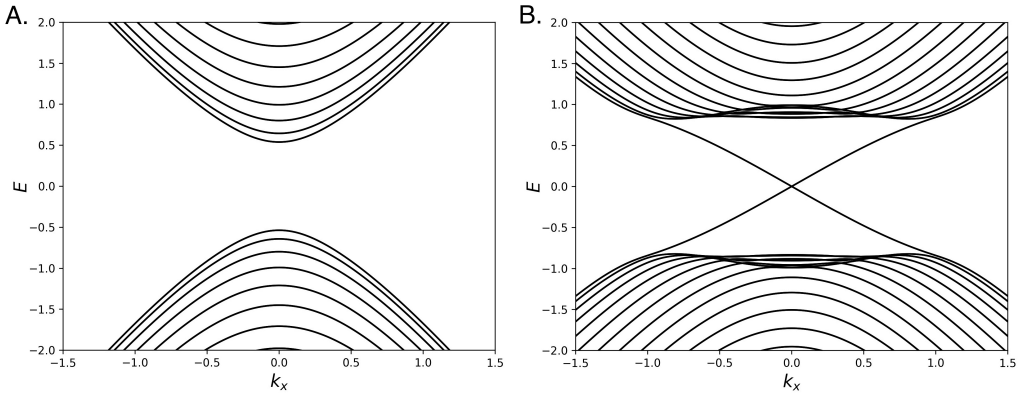

Figure 2.7: The dispersion relation for the quantum wells. (a) When $d < d_c$, HgTe layer behaves as a regular insulator with an energy gap. (b) When $d > d_c$, however, conducting edge states connect the valence and conduction bands.

2.2.5. Berry Phase and Berry Curvature

We can consider the Hamiltonian of a quantum mechanical system, $H(x, \lambda)$, where x is the degrees of freedom of the system, such as position or spin, and λ denoting the parameters of the system, which are determined by external influences, such as an external magnetic field. Given that these parameters are fixed (meaning that the Hamiltonian is constant in time), we know that an eigenstate $|n\rangle$ picks up a phase factor under time evolution:

$$|n\rangle \to e^{-iE_n t/\hbar} |n\rangle \,, \tag{2.32}$$

where E_n is the nth energy eigenvalue. For the sake of simplicity, we assume only non-degenerate cases. If we change the parameters adiabatically, such as the direction of the external magnetic field, the direction of the spin would also change. In this case, the description of the evolution of the particle in Equation 2.32 is not sufficient, for there will be another phase factor upon the path of the process.

Here, we follow the discussion in J.J. Sakurai [27]. Consider the Hamiltonian of a system with an external, time-dependent parameter, denoted as $\lambda(t)$. If λ change in time, from $\lambda(0) = \lambda_0$ to $\lambda(t)$, the time-dependent Schrödinger equation reads:

$$H(\lambda(t)) \, |n(\lambda_0), t_0; t\rangle = i\hbar \frac{\partial}{\partial t} \, |n(\lambda_0), t_0; t\rangle \,, \tag{2.33}$$

where $t_0 = 0$. The adiabatic theorem states that, under an adiabatic process, a particle that starts out in the nth eigenstate of H remains in the nth eigenstate, only picking up a time-dependent phase factor. Therefore, if the change in $\lambda(t)$ is slow enough, we expect

that $|n(\lambda_0), t_0; t\rangle$ will be proportional to $|n(\lambda(t))\rangle$ at time t. Accordingly, we write

$$|n(\lambda_0), t_0; t\rangle = \exp\Big[-\frac{i}{\hbar} \int_0^t E_n(\lambda(t'))dt' \Big] e^{i\gamma_n(t)} \, |n(\lambda(t))\rangle \, . \tag{2.34}$$

The first exponential factor at the right hand side of Equation 2.34 is the familiar term, the build up of phase changes in the stationary states, called the *dynamic phase*. To determine the second phase factor, $e^{i\gamma_n(t)}$, we substitute the Equation 2.34 into 2.33 to obtain

$$\frac{d}{dt}\gamma_n(t) = i \, \langle n(\lambda(t))|\nabla_\lambda n(\lambda(t))\rangle \, \frac{d}{dt}\lambda(t). \tag{2.35}$$

Integrating both sides, we get

$$\gamma_n(t) = i \int_{\lambda_0 \, \mathrm{C}}^{\lambda(t)} \langle n(\lambda(t'))|\nabla_\lambda n(\lambda(t'))\rangle \, d\lambda(t'), \tag{2.36}$$

where C denotes the path of the adiabatic process, as the external parameter changes from λ_0 to $\lambda(t)$. Simplifying the notation, we write

$$\gamma_n(t) = i \int_{\boldsymbol{\lambda_i} \, \mathrm{C}}^{\boldsymbol{\lambda_f}} \langle \psi_n|\nabla_\lambda \psi_n\rangle \, d\boldsymbol{\lambda}. \tag{2.37}$$

If C is a closed loop in the parameter space, meaning $\boldsymbol{\lambda}$ returning to its starting point after a time interval T, path integral in Equation 2.37 becomes

$$\gamma_n(T) = i \oint_{\mathrm{C}} \langle \psi_n|\nabla_\lambda \psi_n\rangle \, d\boldsymbol{\lambda}. \tag{2.38}$$

$\gamma_n(T)$ is called the *Berry Phase*, named after Michael V. Berry, who gave the first clear and general expression in 1984 [28]. As can be seen above, it comes from the adiabatic change of an external parameter. This phase is dependent on the geometric properties of the parameter space, and thus sometimes called as the *geometric phase*. Same applies for topological insulators; Berry phase becomes the phase that an eigenfunction of the Hamiltonian gains when some parameter is adiabatically changed.

If the sample has translational symmetry, then we can label the states by their momentum $\mathbf{k}$. For electrons in a periodic potential, such as in a crystal, the states can be described by Bloch wave functions [29]:

$$\psi_{\mathbf{k}}(\mathbf{r}) = e^{i\mathbf{k}\cdot\mathbf{r}} u_{\mathbf{k}}(\mathbf{r}), \quad u_{\mathbf{k}}(\mathbf{r}+\mathbf{R}) = u_{\mathbf{k}}(\mathbf{r}), \tag{2.39}$$

where $u_{\mathbf{k}}(\mathbf{r})$ is the eigenstate of the periodic Bloch hamiltonian

$$H(\mathbf{k}) = e^{i\mathbf{k}\cdot\mathbf{r}} H e^{-i\mathbf{k}\cdot\mathbf{r}}.$$

$H(\mathbf{k})$, and its eigenvectors and eigenvalues, $|u_n(\mathbf{k})\rangle$ and $E_n(\mathbf{k})$, together define the band

structure. Translational symmetry means $H(\mathbf{k}+\mathbf{K}) = H(\mathbf{k})$, where $\mathbf{K}$ is the reciprocal lattice vector. As a result, the [periodic] Brillouin zone, in which the crystal momentum is defined, now becomes a *torus*. The Bloch wavefunctions are invariant under transformation $|u(\mathbf{k})\rangle \rightarrow e^{i\phi(\mathbf{k})}|u(\mathbf{k})\rangle$. The integrand in Equation 2.38 can be redefined as

$$\mathbf{A} = -i\langle u(\mathbf{k})|\nabla_{\mathbf{k}}|u(\mathbf{k})\rangle\,, \tag{2.40}$$

similar to the electromagnetic vector potential. This is called the *Berry connection*. Under the transformation given above, it transforms as $\mathbf{A} \rightarrow \mathbf{A} + \nabla_{\mathbf{k}}\phi(\mathbf{k})$. We now redefine the Berry phase:

$$\gamma_C = \oint_C \mathbf{A}\cdot d\mathbf{k} = \int_S \mathcal{F} d^2\mathbf{k}, \tag{2.41}$$

where $\mathcal{F} = \nabla \times \mathbf{A}$ is the *Berry curvature*. For example, for a simple two level Hamiltonian, the integration of the Berry curvature over a closed surface gives the Chern number, which is a topological invariant, given as

$$\nu = \frac{1}{2\pi}\int_S \mathcal{F} d^2\mathbf{k}. \tag{2.42}$$

.

2.3. Hyperfine Interaction

In this section, we briefly describe the Hyperfine (HF) coupling, a type of interaction by which the spinful nuclei of a sample couples with the helical edge states, breaking the TR symmetry, and removing the topological protection as a result [30, 31].

Like the spin-orbit (SO) interaction, the hyperfine (HF) coupling is also due to the magnetic torque that is exerted on the electron because of the nucleus. Only this time, the nucleus does not give rise to a magnetic field because of its circular motion around the electron in the electron's reference frame, but because of its magnetic moment due to its spin. The magnetic moments of the proton and electron are given as

$$\boldsymbol{\mu}_p = \frac{g_p e}{2m_p}\mathbf{S}_p, \quad \text{and} \quad \boldsymbol{\mu}_e = \frac{e}{m_e}\mathbf{S}_e, \tag{2.43}$$

where g_p is the gyromagnetic ratio for the proton [32]. The dipole moment of the proton is much smaller than that of the electron because of its large mass term in the denominator. According to the classical electrodynamics, the magnetic field due to a dipole moment, $\boldsymbol{\mu}$, is given as

$$\mathbf{B} = \frac{\mu_0}{4\pi r^3}[3(\boldsymbol{\mu}\cdot\hat{r})\hat{r} - \boldsymbol{\mu}] + \frac{2\mu_0}{3}\boldsymbol{\mu}\delta^3(\mathbf{r}). \tag{2.44}$$

The Hamiltonian for the interaction is $H = -\boldsymbol{\mu} \cdot \mathbf{B}$, as mentioned in Section 2.2.3. Thus the Hamiltonian becomes

$$H_{hf} = \frac{\mu_0 g_p e^2}{8\pi m_p m_e} \cdot \frac{3(\mathbf{S}_p \cdot \hat{r})(\mathbf{S}_e \cdot \hat{r}) - \mathbf{S}_p \cdot \mathbf{S}_e}{r^3} + \frac{\mu_0 g_p e^2}{3 m_p m_e} \mathbf{S}_p \cdot \mathbf{S}_e \delta^3(\mathbf{r}). \tag{2.45}$$

Just like the spin-orbit interaction involves the dot product of the spin of electron, **S**, and the angular momentum of the nucleus, **L**, the hyperfine interaction involves the dot product of the spins of both the electron and the nucleus, hence this interaction is sometimes called the "spin-spin" coupling. More detailed discussions regarding the subject can be found in Dyakonov [32] and Slichter [33].

Although often weak, HF interactions can have significant effects in condensed matter systems, including limiting the coherence of electron spins in quantum dots [34, 35], and causing nuclear spin ordering in 1D [36, 37] and 2D [38, 39] nanostructures. In our case, since the HF coupling intrinsically breaks TR symmetry, it removes topological protection by enabling the backscattering of the helical edge states, which fuels our motivation to calculate backscattering probabilities of the helical edge states and the corresponding polarization of the nuclei.

2.4. Scattering Matrix in Simple 1D Systems

In this section, we briefly introduce and discuss the scattering matrix in 1D, which describes the quantum mechanical scattering effect by relating the incoming quantum states to outgoing quantum states in a 1D system with a scatterer. Here, "incoming" and "outgoing" refer to the states that are propagating towards the scatterer from infinity and away from the scatterer to infinity.

Consider a 1D system with a local potential, depicted as a square barrier for simplicity in Figure 2.8. This can be an impurity, a spinful nucleus, a quantum well, and so on. If we have two incoming waves from both sides, they will partially reflect and partially transmit from the potential. We call the incoming waves from left and right as ψ_L and ψ_R, respectively. The outgoing wave from the left side will be a sum of the reflected part of ψ_L and the transmitted part of ψ_R. Same holds for the right. Therefore, they can be written as

$$\begin{aligned} \phi_L &= r\psi_L + t'\psi_R, \\ \phi_R &= t\psi_L + r'\psi_R, \end{aligned} \tag{2.46}$$

where ϕ_L and ϕ_R are the outgoing waves, r, r' and t, t' are the reflection and transmission

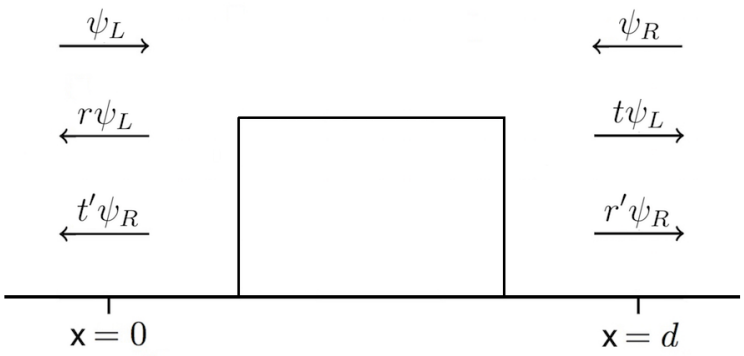

Figure 2.8: A simple potential in a 1D system with two incoming wave functions.

amplitudes, respectively. We can rewrite the equations in (2.46) as

$$\begin{bmatrix} \phi_L \\ \phi_R \end{bmatrix} = \begin{bmatrix} r & t' \\ t & r' \end{bmatrix} \begin{bmatrix} \psi_L \\ \psi_R \end{bmatrix}, \tag{2.47}$$

where the matrix in the middle is called the *scattering matrix*, or the S-matrix in short, because it connects the incoming waves to the outgoing ones in terms of reflection and transmission amplitudes. A more comprehensive treatment can be found in Datta [40], and in Mello and Kumar [41].

Chapter 3

NUCLEAR POLARIZATION

Time-reversal symmetry plays a vital role in securing the virtually perfect robustness of the edge states in a topological insulator device [12, 25, 42, 43]. Having said that, many topological insulators contain spinful nuclei, breaking time-reversal symmetry via hyperfine coupling to the helical edge states, hence destroying the topological protection [44].

Dynamic nuclear polarization, on the other hand, is a process of creating non-equilibrium nuclear spin alignments, resulting from spin transfer between electrons and the nuclei via hyperfine coupling [45]. Therefore, hyperfine coupling has an effect of building up dynamic nuclear polarization in semiconductors [46]. This considerably increases the complexity of the problem, since it is very difficult to model dynamic nuclear polarization due to its many-body nature. Despite the use of approximate methods in certain cases [47], dynamic nuclear polarization has remained as a formidable problem in many condensed matter systems, such as quantum dots [48, 49]. In this chapter, we present the mathematical formulation of the problem, along with the probability amplitudes for single-nucleus interaction. As a result, we obtain a useful phase relation between reflection and transition amplitudes which we later exploit in our numerical analysis.

3.1. The Hamiltonian

We use Fermi point contact interaction for the hyperfine coupling [33, 44], and model our system by the Hamitonian

$$H(x) = -i\hbar v_0 \partial_x \sigma_z + \sum_{n=1}^{N} H_n^{\mathrm{HF}}(x). \tag{3.1}$$

The first part governs the helical edge states, where v_0 is the effective velocity of the electron and σ_i are the Pauli matrices for the electron. Since $-ih\partial_x$ is simply the momentum operator in the x-direction, the tensor product $p_x\sigma_z$ represents the spin-momentum locked nature of the edge states: a right moving electron must have an up-spin, while a left moving electron must have a down-spin. It is present everywhere in the 1D channel,

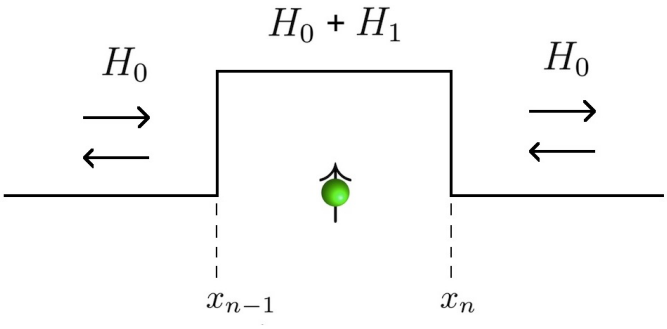

Figure 3.1: The Hamiltonian around the interaction region that is centered by the nth nuclear spin. x_{n-1} and x_n are the left and right endpoints of the interaction region, which is depicted as a square barrier.

including the inside and the outside of the interaction region. The second term captures the hyperfine interaction, where N is the number of nuclear spins present in the channel. We assume that the nuclei are sparse enough so that the hyperfine effect is significant only inside the region determined by the effective size of the Fermi contact interaction, as shown in Figure 3.1. To write the hyperfine term explicitly, we use the real space transformation of an estimation of the hyperfine coupling made for the BHZ model, derived by Lunde and Platero [44], which is averaged over the locations of the nuclei. We obtain

$$H_n^{\text{HF}} = F(x - \frac{x_n + x_{n-1}}{2})[A_\parallel \sigma_z \tau_z^n + A_\perp(\sigma_- \tau_+^n + \sigma_+ \tau_-^n)], \tag{3.2}$$

where σ_i and τ_i^n are the Pauli matrices for electron and the nth nuclear spin, $\sigma_+ = \sigma_x + i\sigma_y$ and $\sigma_- = \sigma_x - i\sigma_y$. It is important to note that τ^n and $\tau^{n'}$ are not in the same space, since every additional nuclear spin doubles the size of the full Hamiltonian. The factors $A_\parallel$ and $A_\perp$ stand for anisotropic coupling for parallel $(+z)$ and perpendicular $(+x)$ directions, respectively. F is the spatial form factor, given by $F(\delta) = \Theta(w/2 - |\delta|)/w$, where Θ is the square barrier step function of width $w = x_n - x_{n-1}$, and unit area spanning the interaction region. Its center falls onto the nucleus. Note that all the products between Pauli matrices are outer products. Because the hyperfine interaction can be considered as "spin-spin" coupling, it is manifested in the Hamiltonian as the product of spins of the electron and the nucleus.

3.2. Hamiltonian in the Matrix Form

We can rewrite our Hamiltonian in Equation 3.1 for a single nuclear spin as $H = H_0 + H_1$, with

$$H_0 = pv_0 \sigma_z \tau_0 \quad \text{and} \quad H_1 = F[A_\parallel \sigma_z \tau_z + A_\perp(\sigma_- \tau_+ + \sigma_+ \tau_-)], \tag{3.3}$$

where τ_0 is the 2×2 identity matrix. In order to obtain the eigenvectors and the eigenvaules, we write the Hamiltonian in the matrix form. When $N = 1$, i.e., for a single nuclear spin, we define our basis vectors $|m_e m_I\rangle$ as

$$|\uparrow\uparrow\rangle = \begin{bmatrix} 1 \\ 0 \\ 0 \\ 0 \end{bmatrix}, \quad |\uparrow\downarrow\rangle = \begin{bmatrix} 0 \\ 1 \\ 0 \\ 0 \end{bmatrix}, \quad |\downarrow\uparrow\rangle = \begin{bmatrix} 0 \\ 0 \\ 1 \\ 0 \end{bmatrix}, \quad |\downarrow\downarrow\rangle = \begin{bmatrix} 0 \\ 0 \\ 0 \\ 1 \end{bmatrix}, \tag{3.4}$$

where m_e is the electron spin and m_I is the nuclear spin. In this basis, we first write H_0:

$$H_0 = pv_0\sigma_z\tau_0 = \begin{bmatrix} pv_0 & 0 & 0 & 0 \\ 0 & pv_0 & 0 & 0 \\ 0 & 0 & -pv_0 & 0 \\ 0 & 0 & 0 & -pv_0 \end{bmatrix}. \tag{3.5}$$

The energy eigenvalues of H_0 are

$$\lambda_{1,2} = pv_0, \quad \lambda_{3,4} = -pv_0, \quad \text{where} \quad p = \hbar k \;\rightarrow\; k = \frac{E}{hv_0}, \tag{3.6}$$

and the eigenvectors become

$$|\phi_{\uparrow\uparrow}\rangle = c_1 \begin{bmatrix} 1 \\ 0 \\ 0 \\ 0 \end{bmatrix} e^{ikx}, \;\; |\phi_{\uparrow\downarrow}\rangle = c_2 \begin{bmatrix} 0 \\ 1 \\ 0 \\ 0 \end{bmatrix} e^{ikx}, \;\; |\phi_{\downarrow\uparrow}\rangle = c_3 \begin{bmatrix} 0 \\ 0 \\ 1 \\ 0 \end{bmatrix} e^{-ikx}, \;\; |\phi_{\downarrow\downarrow}\rangle = c_4 \begin{bmatrix} 0 \\ 0 \\ 0 \\ 1 \end{bmatrix} e^{-ikx}. \tag{3.7}$$

Next, we obtain H_1:

$$H_1 = \begin{bmatrix} FA_\parallel & 0 & 0 & 0 \\ 0 & -FA_\parallel & FA_\perp & 0 \\ 0 & FA_\perp & -FA_\parallel & 0 \\ 0 & 0 & 0 & FA_\parallel \end{bmatrix}. \tag{3.8}$$

Combining H_0 and H_1 together, we obtain the full Hamiltonian:

$$H = \begin{bmatrix} FA_\parallel + pv_0 & 0 & 0 & 0 \\ 0 & -FA_\parallel + pv_0 & FA_\perp & 0 \\ 0 & FA_\perp & -FA_\parallel - pv_0 & 0 \\ 0 & 0 & 0 & FA_\parallel - pv_0 \end{bmatrix}. \tag{3.9}$$

Notice that we have off-diagonal elements only in the middle block, due to Fermi contact interaction exchanging angular momentum between nuclear spin and the electron spin. The eigenvalues are

$$\lambda_{1,4} = \gamma \pm \alpha \quad \text{and} \quad \lambda_{2,3} = -\gamma \pm \sqrt{\alpha^2 + \beta^2}, \tag{3.10}$$

where $\alpha = pv_0$, $\beta = FA_\perp$, and $\gamma = FA_\parallel$. Accordingly, the eigenvectors are given by

$$|\psi_1\rangle = d_1 \begin{bmatrix} 1 \\ 0 \\ 0 \\ 0 \end{bmatrix} e^{ikx} e^{-i\gamma/\hbar v_0}, \quad |\psi_2\rangle = d_2 \begin{bmatrix} 0 \\ \dfrac{\alpha + \sqrt{\alpha^2 + \beta^2}}{\hbar v_0} \\ 1 \\ 0 \end{bmatrix} (e^{iKx} + e^{-iKx}), \tag{3.11}$$

$$|\psi_3\rangle = d_3 \begin{bmatrix} 0 \\ \dfrac{\alpha - \sqrt{\alpha^2 + \beta^2}}{\hbar v_0} \\ 1 \\ 0 \end{bmatrix} (e^{iKx} + e^{-iKx}), \quad |\psi_4\rangle = d_4 \begin{bmatrix} 0 \\ 0 \\ 0 \\ 1 \end{bmatrix} e^{-ikx} e^{i\gamma/\hbar v_0}, \tag{3.12}$$

where

$$K_{1,4} = \pm \frac{E - \gamma}{\hbar v_0} = \pm (k - \frac{\gamma}{\hbar v_0}) \quad \text{and} \quad K_{2,3} = \pm \frac{\sqrt{(E + \gamma)^2 - \beta}}{\hbar v_0} \equiv \pm K. \tag{3.13}$$

The coefficients c_{1-4} and d_{1-4} can be found with a simple boundary matching process for two sides of the interaction region, i.e., x and x', considering that the wavefunctions and their first derivatives will be continous at x and x'.

3.3. Probability Amplitudes for Single-Nucleus Scattering

The hyperfine coupling between the electron and the nucleus breaks time-reversal symmetry for both the electron and the nucleus. However, a joint time-reversal symmetry that flips both spins is preserved. We call this time-reversal symmetry "global" time-reversal invariance. Specifically, if the incident electron and the encountered nuclear spins are parallel, that is, both are up or both are down, the electron simply passes and as a result picks up a pure phase p, to which we will refer to as a "pass". On the other hand, if the incident electron and the nuclear spins are anti-parallel, i.e., one is up and the other is down, the electron will either transit or backscatter. In the transition case, the electron passes without any spin flip, as dictated by spin-orbit coupling and thereby spin-momentum locking. In the backscattering case, however, both spins are flipped. This is because the hyper-

fine interaction causes the electron to backscatter, spin-momentum locking (via spin-orbit coupling) causes the electron spin to be flipped, and the conservation of the total angular momentum causes the nuclear spin to be flipped. As a result, global time-reversal symmetry is preserved. We denote the reflection amplitude by r, and the transition amplitude by t. In all three cases, the total angular momentum is conserved.

Following Russo *et al.* [50], we denote the probability amplitude of the wavefunction by $\psi_{m_e,m_I}(x)$, where m_e and m_I are the electronic and nuclear spins, x_{n-1} and x_n are locations of the left and right endpoints of the interaction region that is centered by the nth nuclear spin, respectively. The amplitude for the "pass" of an electron is described by

$$\frac{\psi_{\uparrow\uparrow}(x_n)}{\psi_{\uparrow\uparrow}(x_{n-1})} = \frac{\psi_{\downarrow\downarrow}(x_{n-1})}{\psi_{\downarrow\downarrow}(x_n)} = p, \tag{3.14}$$

while the transition amplitude is

$$\frac{\psi_{\uparrow\downarrow}(x_n)}{\psi_{\uparrow\downarrow}(x_{n-1})} = \frac{\psi_{\downarrow\uparrow}(x_{n-1})}{\psi_{\downarrow\uparrow}(x_n)} = t. \tag{3.15}$$

For both p and t, the amplitudes are the same for the electrons incoming from right and left, since the global time-reversal symmetry is preserved. The reflection amplitude, on the other hand, is described by

$$\frac{\psi_{\downarrow\uparrow}(x_{n-1})}{\psi_{\uparrow\downarrow}(x_{n-1})} = r_{\hookleftarrow} \quad \text{and} \quad \frac{\psi_{\uparrow\downarrow}(x_n)}{\psi_{\downarrow\uparrow}(x_n)} = r_{\hookrightarrow}, \tag{3.16}$$

where $r_{\hookleftarrow}$ denoting reflection from the left side of the impurity. We also have

$$|r_{\hookleftarrow}|^2 = |r_{\hookrightarrow}|^2 \equiv |r|^2 = 1 - |t|^2. \tag{3.17}$$

We want to check whether there is any relation between r and t that we can exploit in our calculations. To that end, we examine the behavior of the eigenstates under the action of global time-reversal symmetry operator. First, we write the wavefunctions in terms of the probability amplitudes, p, t, and r, in the position basis [51]. The eigenstates of the parallel cases are straightforward, they are the eigenvectors of the Hamiltonian multiplied by the "pass" amplitude:

$$\langle x|\psi_{\uparrow\uparrow}\rangle = \begin{bmatrix} e^{ipx} \\ 0 \\ 0 \\ 0 \end{bmatrix}, \quad \langle x'|\psi_{\uparrow\uparrow}\rangle = \begin{bmatrix} p_{\rightarrow}e^{ipx'} \\ 0 \\ 0 \\ 0 \end{bmatrix}, \tag{3.18}$$

$$\langle x|\psi_{\downarrow\downarrow}\rangle = \begin{bmatrix} 0 \\ 0 \\ 0 \\ p_{\leftarrow}e^{-ipx} \end{bmatrix}, \quad \langle x'|\psi_{\downarrow\downarrow}\rangle = \begin{bmatrix} 0 \\ 0 \\ 0 \\ e^{-ipx'} \end{bmatrix}. \tag{3.19}$$

where x denotes the left side of the nucleus, i.e., the magnetic impurity, and x' denoting the right. Similarly $p_{\rightarrow}$ is the amplitude for passing from the left, while $p_{\leftarrow}$ is for passing from the right. For instance, if both spins are up and the electron is at the right side of the impurity, the only possible scenario is that the electron has just passed the impurity, because spin-momentum locking forces it to be a right moving electron. Therefore $\langle x'|\psi_{\uparrow\uparrow}\rangle$ will be as shown in Equation 3.18.

The anti-parallel cases are a bit more involved. They are given by

$$\langle x|\psi_{\uparrow\downarrow}\rangle = \begin{bmatrix} 0 \\ e^{ipx} \\ 0 \\ 0 \end{bmatrix} + \begin{bmatrix} 0 \\ 0 \\ r_{\hookleftarrow}e^{-ipx} \\ 0 \end{bmatrix} = \begin{bmatrix} 0 \\ e^{ipx} \\ r_{\hookleftarrow}e^{-ipx} \\ 0 \end{bmatrix}, \quad \langle x'|\psi_{\uparrow\downarrow}\rangle = \begin{bmatrix} 0 \\ t_{\rightarrow}e^{ipx'} \\ 0 \\ 0 \end{bmatrix}, \tag{3.20}$$

$$\langle x|\psi_{\downarrow\uparrow}\rangle = \begin{bmatrix} 0 \\ 0 \\ t_{\leftarrow}e^{-ipx} \\ 0 \end{bmatrix}, \quad \langle x'|\psi_{\downarrow\uparrow}\rangle = \begin{bmatrix} 0 \\ r_{\hookrightarrow}e^{ipx'} \\ 0 \\ 0 \end{bmatrix} + \begin{bmatrix} 0 \\ 0 \\ e^{-ipx'} \\ 0 \end{bmatrix} = \begin{bmatrix} 0 \\ r_{\hookrightarrow}e^{ipx'} \\ e^{-ipx'} \\ 0 \end{bmatrix}. \tag{3.21}$$

Again, $t_{\rightarrow}$ and $r_{\hookleftarrow}$ denote transition and reflection from the left, respectively. As an example, consider $\langle x|\psi_{\uparrow\downarrow}\rangle$. Since the electron is at the left and moving to the right, the eigenstate will be a combination of it approaching to the impurity and reflected from it (transition can not be the case, since the electron is on the left). Hence it is the sum of the basis kets $|\uparrow\downarrow\rangle$ and $r_{\rightarrow}$ times $|\downarrow\uparrow\rangle$, since the reflection would cause the spins to flip. As another example, consider $\langle x'|\psi_{\uparrow\downarrow}\rangle$. Because the electron is at the right and moving to the right, the eigenstate is simply $t_{\rightarrow}$ times the basis ket $|\psi_{\uparrow\downarrow}\rangle$, as it is transmited from the left.

We now define the TR operator as $\mathcal{T}_{1/2} = i\sigma_y\mathcal{K}$, where $\mathcal{K}$ is the complex conjugation operator. In the case of the spin $1/2$ impurity, the operator for global time-reversal symmetry operator takes the form $\mathcal{T}_{GTR} = (\mathcal{T}_{1/2} \otimes \mathcal{T}_{1/2})\mathcal{K}$, assuming the nucleus has 1/2 spin.

Explicitly:

$$\mathcal{T}_{GTR} = \left[i \begin{pmatrix} 0 & -i \\ i & 0 \end{pmatrix} \right] \otimes \left[i \begin{pmatrix} 0 & -i \\ i & 0 \end{pmatrix} \right] \mathcal{K} = \begin{bmatrix} 0 & 0 & 0 & 1 \\ 0 & 0 & -1 & 0 \\ 0 & -1 & 0 & 0 \\ 1 & 0 & 0 & 0 \end{bmatrix} \mathcal{K}. \tag{3.22}$$

If we apply $\mathcal{T}_{GTR}$ to the eigenstate $\langle x|\psi_{\uparrow\uparrow}\rangle$, we obtain

$$\langle x|\mathcal{T}_{GTR}|\psi_{\uparrow\uparrow}\rangle = \begin{bmatrix} 0 & 0 & 0 & 1 \\ 0 & 0 & -1 & 0 \\ 0 & -1 & 0 & 0 \\ 1 & 0 & 0 & 0 \end{bmatrix} \mathcal{K} \begin{bmatrix} e^{ipx} \\ 0 \\ 0 \\ 0 \end{bmatrix} = \begin{bmatrix} 0 \\ 0 \\ 0 \\ e^{-ipx} \end{bmatrix}. \tag{3.23}$$

$\langle x|\mathcal{T}_{GTR}|\psi_{\uparrow\uparrow}\rangle$ must be proportional to $\langle x|\psi_{\downarrow\downarrow}\rangle = [0 \quad 0 \quad 0 \quad p_{\leftarrow}e^{-ipx}]^T$. In the same manner, $\langle x'|\mathcal{T}_{GTR}|\psi_{\uparrow\uparrow}\rangle$ and $\langle x'|\psi_{\downarrow\downarrow}\rangle$ must also be proportional. Therefore we conclude:

$$p_{\rightarrow} = p_{\leftarrow} \equiv p, \quad \text{where} \quad |p|^2 = 1 \tag{3.24}$$

as we asserted before, right after Equation 3.14. We now apply $\mathcal{T}_{GTR}$ to the remaining states:

$$\langle x|\mathcal{T}_{GTR}|\psi_{\uparrow\downarrow}\rangle = \begin{bmatrix} 0 \\ -r^*_{\hookleftarrow}e^{ipx} \\ -e^{-ipx} \\ 0 \end{bmatrix}, \quad \langle x|\mathcal{T}_{GTR}|\psi_{\downarrow\uparrow}\rangle = \begin{bmatrix} 0 \\ -t^*_{\leftarrow}e^{ipx} \\ 0 \\ 0 \end{bmatrix}, \tag{3.25}$$

$$\langle x'|\mathcal{T}_{GTR}|\psi_{\uparrow\downarrow}\rangle = \begin{bmatrix} 0 \\ 0 \\ -t^*_{\rightarrow}e^{-ipx'} \\ 0 \end{bmatrix}, \quad \langle x'|\mathcal{T}_{GTR}|\psi_{\downarrow\uparrow}\rangle = \begin{bmatrix} 0 \\ -e^{-ipx'} \\ -r^*_{\hookrightarrow}e^{-ipx'} \\ 0 \end{bmatrix}. \tag{3.26}$$

We see that these states are the superpositions of incoming states from left and right, i.e., the global time-reversal symmetry is blending the eigenstates incoming from the left of the impurity, with those that are incoming from the right. Hence we write the equation

$$\mathcal{T}_{GTR}\,|\psi_{\uparrow\downarrow}\rangle = a_0\,|\psi_{\uparrow\downarrow}\rangle + b_0\,|\psi_{\downarrow\uparrow}\rangle\,. \tag{3.27}$$

Substituting the states in the Equation 3.25 into the Equation 3.27, we get

$$-r^*_{\hookleftarrow} = a_0, \quad -1 = a_0 r_{\hookleftarrow} + b_0 t_{\leftarrow}. \tag{3.28}$$

Substituting the states in the Equation 3.26 into the Equation 3.27, we obtain

$$0 = a_0 t_{\rightarrow} + b_0 r_{\hookrightarrow}, \quad b_0 = -t^*_{\rightarrow}. \tag{3.29}$$

Now we have a_0 and b_0 in terms of transition and reflection amplitudes t and r, we substitute them into the rest of the equations in (3.28) and (3.29), to get

$$-r^*_{\hookleftarrow} r_{\hookleftarrow} - t^*_{\rightarrow} t_{\leftarrow} = -1 \quad \Rightarrow \quad |r_{\hookleftarrow}|^2 + t^*_{\rightarrow} t_{\leftarrow} = 1, \tag{3.30}$$

$$-r^*_{\hookleftarrow} t_{\rightarrow} - t^*_{\rightarrow} r_{\hookrightarrow} = 0 \quad \Rightarrow \quad r^*_{\hookleftarrow} t_{\rightarrow} + r_{\hookrightarrow} t^*_{\rightarrow} = 0. \tag{3.31}$$

We know that $|r_{\hookleftarrow}|^2 = 1 - |t_{\rightarrow}|^2$. Substituting this into Equation 3.30, we can write

$$1 - |t_{\rightarrow}|^2 + t^*_{\rightarrow} t_{\leftarrow} = 1 \quad \Rightarrow \quad |t_{\rightarrow}|^2 = t^*_{\rightarrow} t_{\leftarrow}. \tag{3.32}$$

But this means that $t_{\rightarrow} = t_{\leftarrow}$, as we stated earlier. Hence we define

$$t_{\rightarrow} = t_{\leftarrow} \equiv t = |t| e^{i\phi_t}. \tag{3.33}$$

If the impurity has inversion symmetry, as assumed before, we also write

$$r_{\hookleftarrow} = r_{\hookrightarrow} \equiv r = |r| e^{i\phi_r}. \tag{3.34}$$

Using these expressions, Equation 3.31 now becomes

$$r^* t + r t^* = 0, \tag{3.35}$$

which simply means $\phi_t = \phi_r + \frac{\pi}{2}$. Therefore if we choose r to be real, we have to choose t as purely imaginary in our computational analysis. Since the system is coherent, it does not matter which gauge we choose, as long as the phase difference is constant. In this thesis we ignore phase variations between scatterings.

Chapter 4

ELECTRON AND NUCLEAR SPIN DYNAMICS AT THE TOPOLOGICAL INSULATOR EDGE

In this chapter, we present our calculations for the scattering probabilities of the edge electrons in 1D channels interacting with up to 10 nuclear spins. In order to achieve this, we use a numerical simulation which harnesses single-nucleus scattering amplitudes that are discussed in the preceding chapter to calculate the total reflection probability. We demonstrate a universal trend and briefly discuss its meaning.

4.1. The Case of Multiple Nuclei

In the case of the multiple nuclei ($N > 1$), straightforward approaches to obtain scattering probabilities, such as diagonalization of the Hamiltonian, get immensely difficult, because the size of the Hamiltonian exponentially increases with N. However, we can use the amplitudes for single-nucleus interaction, p, r and t, to calculate the overlap between the initial and final states of the overall system. The ket $\left|\Psi^{(E)}_{\mathbf{m};\rightarrow}\right\rangle$ represents the the eigenstate of an electron incoming from the left, where E is energy and $\mathbf{m} = \{m_n\}$ is initial nuclear spin configuration before the interaction. For instance, for an electron incident from the left with four impurities on its way, with nuclear spins up-down-up-down in the channel, the corresponding state will be $\left|\Psi^{(E)}_{\uparrow\downarrow\uparrow\downarrow;\rightarrow}\right\rangle$. After the electron enters the multi-nuclear region, it will pass, transmit, or reflect from each impurity in accord with the single-nucleus analysis provided in the previous section. After interacting with all, or some, of the impurities, it will depart the nuclear region either from the left, where it came from, or from the right, depending on the amplitudes r and t. We will refer to the first case as total reflection, and the second case as total transition. We define the outstate as $|x_j; m'_e; \mathbf{m}'\rangle$, where x_j is the position, m_e is the spin of the electron as dictated by conservation of the total angular momentum, and $\mathbf{m}'$ is the final nuclear spin configuration after all interactions. Then the probability that the system ends up in a particular outstate

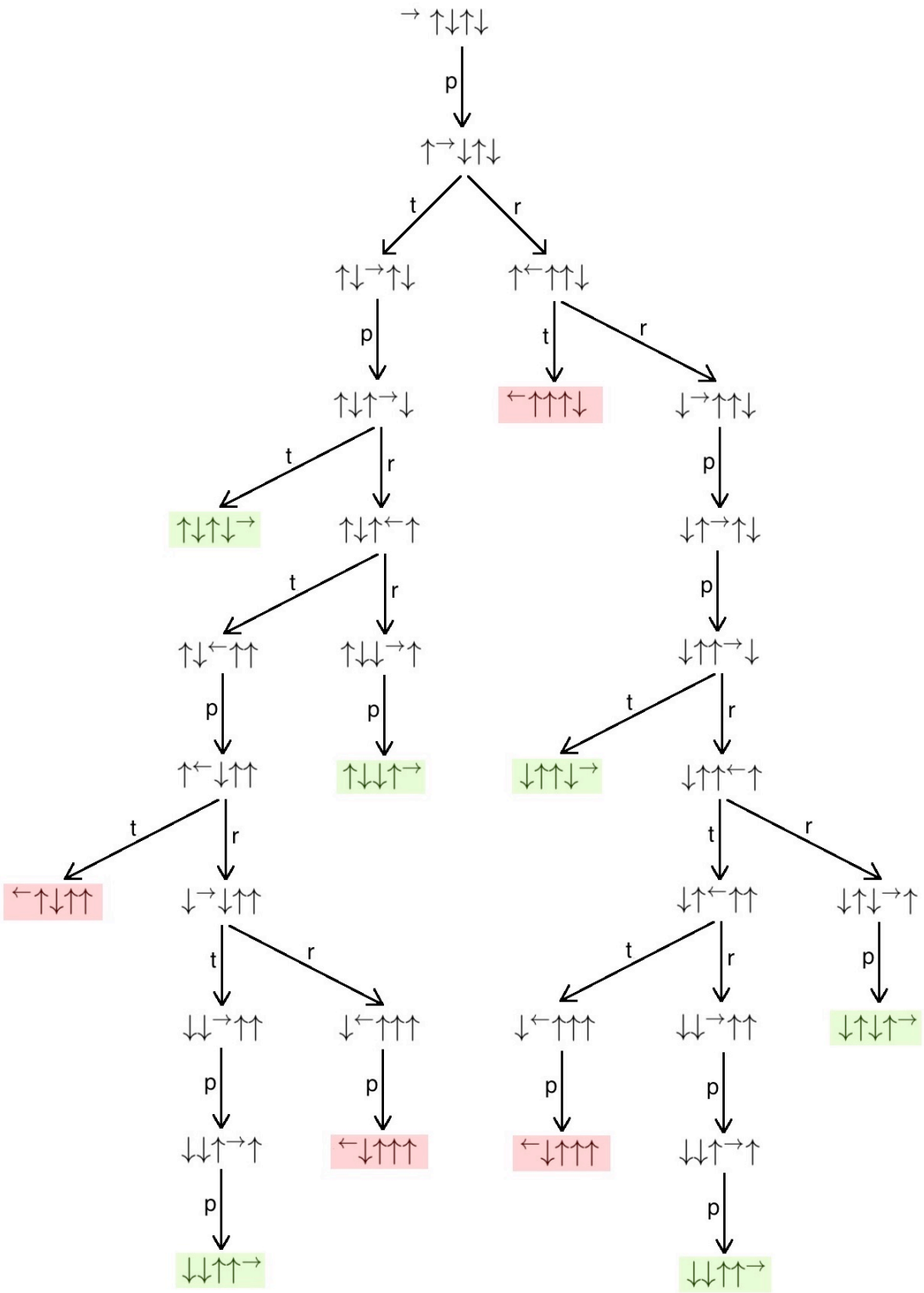

Figure 4.1: An example of the "probability-amplitude tree" of an initial state with an electron incoming from the left to the nuclear spins configured ↑↓↑↓. The electron may depart the nuclear region either from the left or from the right, depending on the single-scattering amplitudes r and t. We are interested only in the incidents of total reflection case, which are highlighted in red.

is given by

$$\mathcal{P}_{\mathbf{m}\mathbf{m}';j} = \left| \left\langle x_j; m_e'; \mathbf{m}' \middle| \Psi^{(E)}_{\mathbf{m};\rightarrow} \right\rangle \right|^2. \tag{4.1}$$

In order to calculate the probabilities, we need to obtain inner product $\left\langle x_j; m_e'; \mathbf{m}' \middle| \Psi^{(E)}_{\mathbf{m};\rightarrow} \right\rangle$ numerically, for different r and t values. However, there are interfering paths to reach a final state from a certain initial state, depending on what happens to the electron inside the region of multiple nuclei. For instance, again consider an electron incoming from the left, which automatically means a spin-up electron due to spin-momentum locking. If it encounters four impurities with spins $\uparrow\downarrow\uparrow\downarrow$, it will certainly pass the first one, as the spins are parallel. However, it can either transmit or reflect from the second one, since their spins are anti-parallel. This leads to two possible future paths, and goes on in a similar fashion. Hence, what we get is a probability tree, as depicted in Figure 4.1. There is a different tree for each initial state, with multiple final states. Since each encounter is governed by single-nucleus scattering amplitudes p, r, and t, finding the amplitude for an initial state that ends up in a particular final state, therefore finding the inner product $\left\langle x_j; m_e'; \mathbf{m}' \middle| \Psi^{(E)}_{\mathbf{m};\rightarrow} \right\rangle$, amounts to successively multiplying the amplitudes p, r, and t along the path connecting the initial and final states, and summing over all such paths. Hence the inner product is given by

$$\left\langle x_j; m_e'; \mathbf{m}' \middle| \Psi^{(E)}_{\mathbf{m};\rightarrow} \right\rangle = \sum_{\Gamma_{\mathbf{m},\mathbf{m}'}} \prod_n r_n^{N_{r_n}[\Gamma_{\mathbf{m},\mathbf{m}'}]} p_n^{N_{p_n}[\Gamma_{\mathbf{m},\mathbf{m}'}]} t_n^{N_{t_n}[\Gamma_{\mathbf{m},\mathbf{m}'}]}, \tag{4.2}$$

where $N_{r_n}[\Gamma]$ is the number of reflections from the nth impurity along path Γ. $N_{t_n}[\Gamma]$ and $N_{p_n}[\Gamma]$ are defined in the same fashion. In order to determine the probabilities of total reflection numerically, we developed a Python code. We provide the details of the code in the Appendix. The code calculates the probabilities of total transition and reflection. We focus on the total reflection case. Moreover, we assume unpolarized nuclear spins, i.e., we consider the nuclear spin configurations with total angular momentum zero, containing an equal number of up and down spins. Without loss of generality, we assume that the incoming electron is incident from the left, because the result for a chiral configuration with an electron incoming from right will exactly be the same, due to the global time-reversal symmetry.

4.2. Calculating the Probability of Total Reflection

We numerically calculate the formula given in Equation 4.2 to obtain the inner products. We then sum the squares of amplitudes for each possible initial configuration, then

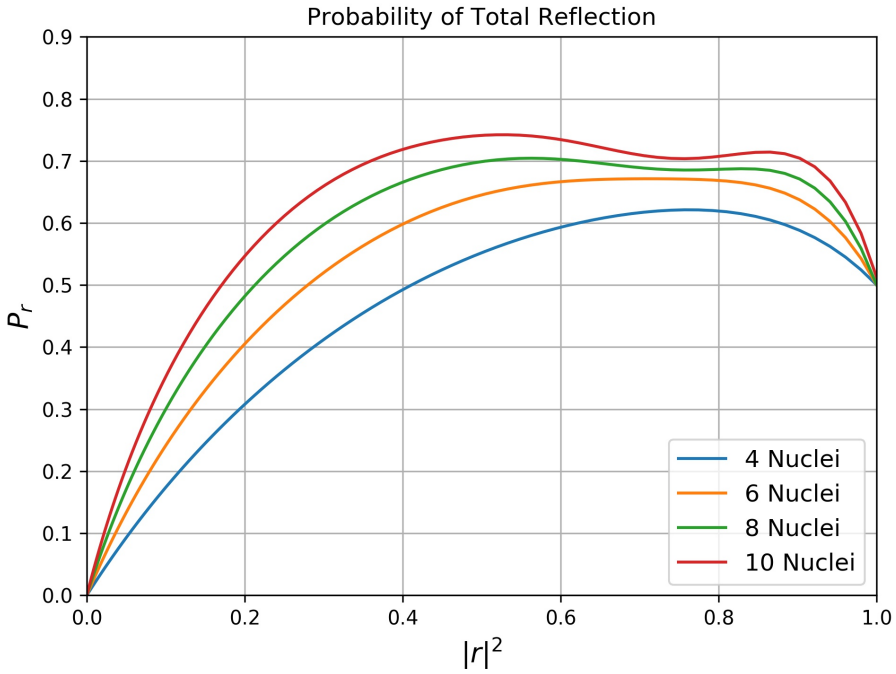

Figure 4.2: Probability of total reflection plots for nuclear spins up to $N = 10$. All possible nuclear spin configurations with zero total polarization are included and averaged over, except for $N = 10$. (Due to unpractical computation times, 6 initial configurations among total 252, are excluded for the $N = 10$ case.)

successively sum and take the average over all possible initial configurations, since the distribution of nuclear spins will statistically be random in a realistic system without any bias. This way, we obtain the probability of total reflection for a given value of $|r|^2$. We choose r as real and t as purely imaginary, due to the $\pi/2$ phase difference between these amplitudes, as shown in Equation 3.35. Since the electron will certainly pass a parallel spin impurity and we know $|p|^2 = 1$ from Equation 3.24, we take $p = 1$ for simplicity. We obtain and plot the probabilities of total reflection, P_r, as a function of $|r|^2$, for nuclear configurations up to 10 spins, as shown in Figure 4.2.

Before we go on to comment on probability plots in Figure 4.2, we first consider the extreme cases of the perfect conductor and the perfect scatterer, where $|r|^2 = 0$ and $|r|^2 = 1$, respectively. The first case would mimic a regular topological insulator with vanishing hyperfine interaction. However, in the second case, i.e., the perfect scatterer limit, the system behaves essentially classical, as all branchings disappear. For instance, for an electron incoming from the left, if the first impurity has an up-spin, it is certain that the electron will transmit through all interaction region and depart from the right, regardless of the spin configuration of the rest of nuclei. This is because the electron ($S_e = \uparrow$) will proceed until encountering the first anti-parallel spin ($S_n = \downarrow$), reflect from it, flips the impurity ($S_n = \uparrow$) and get flipped ($S_e = \downarrow$), but this means that it will immediately encounter the one it just passed ($S_{n-1} = \uparrow$). Now that they are anti-parallel, it will reflect

back, and transmits through $S_n = \uparrow$, and goes on like that. If the first impurity has a down-spin however, the electron will certainly reflect back and depart from the left. For our case, where an equal number of up and down spins are present, this means that the overall probability of total reflection automatically becomes 1/2, as can be seen from Figure 4.2, where all curves converge to this value.

The curves for probability of total reflection exhibit some interesting properties. As shown in Figure 4.2, the plots for different number of nuclear spins have extrema, all of which coincide at about $|r|^2 = 0.77$. In particular, the plots for $N = 4$ and $N = 6$ have maxima, whereas the ones for $N = 8$ and $N = 10$ have minima, suggesting a universality at this specific value. This trend can more clearly be seen in Figure 4.3, where the plots for $(1/N)(dP_r/d|r|^2)$ are shown. Unfortunately, we were not able to obtain the plots for higher number of impurities due to computational limitations, since the computation time substantially increases with the increasing number of magnetic impurities. However, Russo *et al.* [50], who performed a similar calculation, observed the same trend persists around a similar value for higher number of nuclei, such as $N = 24$. Taking potential inaccuracies due to numerical calculation into account, a scale invariant, universal extremum at $|r|^2 = 0.75$ seems plausible, considering the system consisting of identical components that come in two types. The actual reason underlying this interesting effect will be the topic of the future work.

Also note that since $N/2$ of the nuclear spins are down, the Taylor expansion of either $|r|^2$ or $|t|^2 = 1 - |r|^2$ is exponential-like with power $N/2$. For $|r|^2 \ll 1$, only the $|r|^2$ term survives, hence the derivative $(1/N)(dP_r/d|r|^2)$ converges to $(1/N)(N/2) = 0.5$ in this regime, as can be seen in Figure 4.3.

We also check which types of initial nuclear spin arrangements contributes most to the extremum. As mentioned earlier, after calculating the absolute squares of the inner products, we calculate the probabilities of total reflection by averaging over all initial states. However, nuclear spin configurations with down spins piled to the further end of the channel have the largest probability trees with the most branches. These configurations also require the longest computation time. In order to see the particular contribution of these configurations to the plots in Figure 4.2, we additionally obtained the plots of total reflection probability for different, individual initial states. Indeed, we find that as the down nuclear spins move to the further end of the nuclear region, the extrema start to be visible, as shown in Figure 4.4. We also find that for a given type of arrangement of nuclear spins, the defining characteristic of probability curves becomes more pronounced as the total number of nuclear spins increase, as most visibly manifested in Figure 4.4 (d).

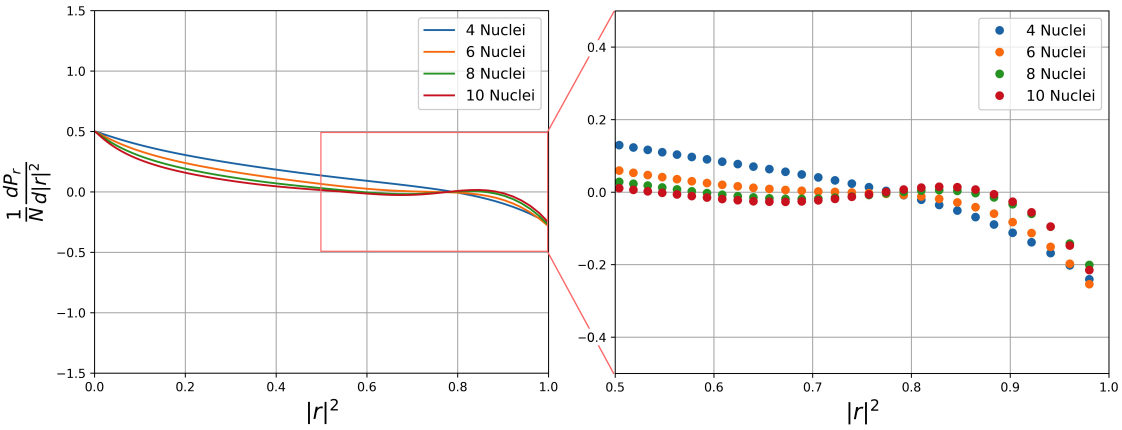

Figure 4.3: Derivative of the probability of total reflection curves, normalized by the number of nuclear spins. All four plots share the same extremum point, which is at about $|r|^2 = 0.77$.

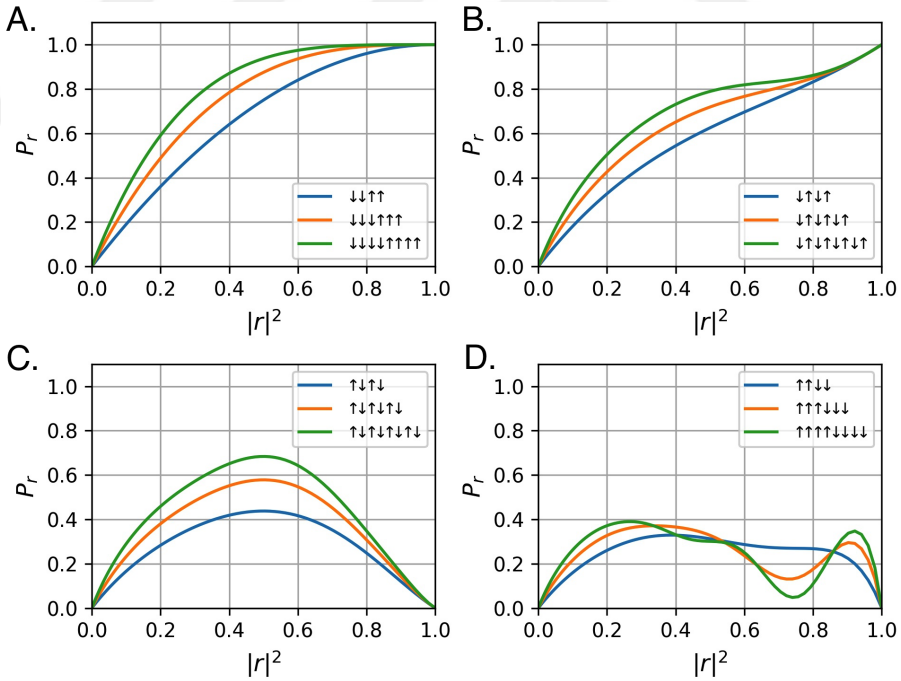

Figure 4.4: Probability of total reflection plots for several individual nuclear spin configurations, including (a) domain wall arrangements with down spins piled up at the left, (b) and (c) antiferromagnet arrangements, and (d) domain wall arrangements with down spins piled up at the right. As the down nuclear spins move to the right end of interaction region, the extrema start to appear, suggesting these states are mostly responsible for the universal extremum. It is also visible that as the system size increases, extrema become more pronounced.

4.3. Concluding Remarks

In this chapter, we presented our results in the form of total reflection probability plots for the edge channels of a quantum spin Hall device. We showed that edge channels with different number of nuclear spins have an extremum at the same point, $|r|^2 = 0.77$, as long as the initial total polarization is zero. We also showed that as the number of nuclear spins increases, the characteristic of any extrema becomes more salient.

The helical edge states in a quantum spin Hall system are topologically protected by the combination of spin-orbit coupling and time-reversal symmetry, where the latter forbids any backscattering of these states. Because the time-reversal symmetry is broken by the nuclear spins, resulting backscattering reduces the conductance in the edges of the quantum spin Hall device [31, 52]. On the other hand, dynamic nuclear polarization enabled by the hyperfine coupling between the electron and nuclear spins can be utilized as a memory resource [46, 53] or even as a rechargable spin battery [46]. For instance, in a recent work where the nuclear spins in a quantum spin Hall device are exploited as a memory resource, the proposed Maxwell's demon application depends on the hyperfine coupling between electron and nuclear spins [54]. The nonmonotonic behaviour of the probability of backscattering of the helical edge electrons shown in Figures 4.2 and 4.4 suggests that coherence plays an important role in the aforementioned systems.

The quantum spin Hall system we have worked on in this thesis provides a convenient medium for spintronic applications. Our results can be applied to any spintronics device that uses topologically protected spin-momentum locked states in 1D, such as a 2D quantum spin Hall insulator with 1D edge modes. Our approach also provides flexibility for systems containing nuclear spins, or any magnetic impurities in general, that spin-momentum locked electronic states may be coupled via hyperfine interaction.

Our results can be expanded by adding a dynamical phase and by randomizing the positions of nuclear spins to further study the interplay between randomness and coherence on such systems. Our work can also be generalized to higher dimensional systems, such as the 2D surface states of a 3D topological insulator, which is currently being studied [55].

Chapter 5

CONCLUSION

In this thesis, we studied back-scattering probabilities of the helical edge electrons in 2D topological insulators, enabled by their hyperfine coupling to the nuclei.

In Chapter 2, we provided a selected survey on topological insulators, as well as the subjects relevant to the background of this thesis.

We started Chapter 3 by solving the Dirac-like Hamiltonian of the system by using Fermi point contact interaction. We introduced the reflection and transition amplitudes, r and t, for single-nucleus-electron interaction, as well as the global time-reversal (GTR) symmetry featured by the system. By examining the behavior of the edge states under GTR symmetry, we showed that there is a phase relation between the amplitudes that we later utilized in our numerical calculations.

In Chapter 4, we introduced a formula that gives the overlap between the initial and final states of the overall system in the case of multiple nuclei, as well as the definition of a total reflection. We explained how our program works to calculate the probability of total reflection for a given reflection amplitude, r, and calculated the probabilities for the whole range of $0 < |r|^2 < 1$, in the presence of multiple nuclei. We reported our results by providing the plots for probability of total reflection, for edge channels containing up to 10 nuclear spins. We found that all the plots have a common extremum at a specific value, $|r|^2 \cong 3/4$, suggesting a universality independent of the system size. We also showed that initial nuclear spin configurations with down spins placed at the further end of nuclear region are the top contributors to possible extrema. We concluded this chapter by discussing the potential use of our findings in future research, including spintronic devices that use topologically protected spin-momentum locked edge states or that utilize nuclear spins as a memory resource via dynamic nuclear polarization.

Bibliography

[1] K. v. Klitzing, G. Dorda, and M. Pepper, "New method for high-accuracy determination of the fine-structure constant based on quantized Hall resistance," *Phys. Rev. Lett.*, vol. 45, p. 494, 1980.

[2] K. von Klitzing, "Developments in the quantum hall effect," *Philosophical Transactions of the Royal Society of London A: Mathematical, Physical and Engineering Sciences*, vol. 363, no. 1834, pp. 2203–2219, 2005.

[3] D. J. Thouless, M. Kohmoto, M. P. Nightingale, and M. den Nijs, "Quantized Hall conductance in a two-dimensional periodic potential," *Phys. Rev. Lett.*, vol. 49, p. 405, 1982.

[4] M. O. Goerbig, "Quantum hall effects," *arXiv preprint arXiv:0909.1998*, 2009.

[5] H. L. Stormer, "Nobel lecture: The fractional quantum Hall effect," *Rev. Mod. Phys.*, vol. 71, p. 875, 1999.

[6] J. Asbóth, L. Oroszlány, and A. Pályi, *A Short Course on Topological Insulators: Band Structure and Edge States in One and Two Dimensions*. Lecture Notes in Physics, Springer International Publishing, 2016.

[7] E. H. Hall, "On a new action of the magnet on electric currents," *American Journal of Mathematics*, vol. 2, no. 3, pp. 287–292, 1879.

[8] P. Drude, "Zur elektronentheorie der metalle," *Annalen der Physik*, vol. 306, no. 3, pp. 566–613, 1900.

[9] J. K. Jain, *Composite fermions*. Cambridge University Press, 2007.

[10] R. Prange and S. Girvin, *The Quantum Hall Effect*. Springer-Verlag, 1990.

[11] R. B. Laughlin, "Quantized Hall conductivity in two dimensions," *Phys. Rev. B*, vol. 23, p. 5632, 1981.

[12] S.-C. Zhang, "Topological states of quantum matter," *Physics*, vol. 1, p. 6, 2008.

[13] D. Thouless, *Topological Quantum Numbers in Nonrelativistic Physics*. World Scientific Publishing Company Pte Limited, 1998.

[14] X.-L. Qi, T. L. Hughes, and S.-C. Zhang, "Topological field theory of time-reversal invariant insulators," *Physical Review B*, vol. 78, no. 19, p. 195424, 2008.

[15] B. A. Bernevig, T. L. Hughes, and S.-C. Zhang, "Quantum spin Hall effect and topological phase transition in HgTe quantum wells," *Science*, vol. 314, no. 5806, p. 1757, 2006.

[16] B. A. Bernevig and S.-C. Zhang, "Quantum spin hall effect," *Physical review letters*, vol. 96, no. 10, p. 106802, 2006.

[17] C. L. Kane and E. J. Mele, "Quantum spin Hall effect in graphene," *Phys. Rev. Lett.*, vol. 95, p. 226801, 2005.

[18] C. Wu, B. A. Bernevig, and S.-C. Zhang, "Helical liquid and the edge of quantum spin hall systems," *Physical review letters*, vol. 96, no. 10, p. 106401, 2006.

[19] C. L. Kane and E. J. Mele, "Z_2 topological order and the quantum spin Hall effect," *Phys. Rev. Lett.*, vol. 95, p. 146802, 2005.

[20] J. J. Sakurai and E. D. Commins, *Modern quantum mechanics, revised edition*. AAPT, 1995.

[21] L. Fu and C. L. Kane, "Topological insulators with inversion symmetry," *Phys. Rev. B*, vol. 76, p. 045302, 2007.

[22] M. König, S. Wiedmann, C. Brüne, A. Roth, H. Buhmann, L. W. Molenkamp, X.-L. Qi, and S.-C. Zhang, "Quantum spin Hall insulator state in HgTe quantum wells," *Science*, vol. 318, no. 5851, p. 766, 2007.

[23] A. Roth, C. Brüne, H. Buhmann, L. W. Molenkamp, J. Maciejko, X.-L. Qi, and S.-C. Zhang, "Nonlocal transport in the quantum spin Hall state," *Science*, vol. 325, no. 5938, p. 294, 2009.

[24] E. O. Kane, "Band structure of indium antimonide," *Journal of Physics and Chemistry of Solids*, vol. 1, no. 4, pp. 249–261, 1957.

[25] X.-L. Qi and S.-C. Zhang, "Topological insulators and superconductors," *Rev. Mod. Phys.*, vol. 83, p. 1057, 2011.

[26] B. Zhou, H.-Z. Lu, R.-L. Chu, S.-Q. Shen, and Q. Niu, "Finite size effects on helical edge states in a quantum spin-hall system," *Physical review letters*, vol. 101, no. 24, p. 246807, 2008.

[27] J. Sakurai and J. Napolitano, *Modern quantum mechanics*. Addison-Wesley, 2010.

[28] M. V. Berry, "Quantal phase factors accompanying adiabatic changes," *Proceedings of the Royal Society of London A: Mathematical, Physical and Engineering Sciences*, vol. 392, no. 1802, p. 45, 1984.

[29] C. Kittel, P. McEuen, and P. McEuen, *Introduction to solid state physics*, vol. 8. Wiley New York, 1996.

[30] C.-H. Hsu, P. Stano, J. Klinovaja, and D. Loss, "Nuclear spin-induced localization of the edge states in two-dimensional topological insulators," *arXiv 1703.03421*, 2017.

[31] A. Del Maestro, T. Hyart, and B. Rosenow, "Backscattering between helical edge states via dynamic nuclear polarization," *Phys. Rev. B*, vol. 87, p. 165440, 2013.

[32] M. I. Dyakonov and A. Khaetskii, *Spin physics in semiconductors*, vol. 157. Springer, 2017.

[33] C. Slichter, *Principles of Magnetic Resonance*. Springer Series in Solid-State Sciences, Springer Berlin Heidelberg, 1996.

[34] A. V. Khaetskii, D. Loss, and L. Glazman, "Electron spin decoherence in quantum dots due to interaction with nuclei," *Phys. Rev. Lett.*, vol. 88, p. 186802, Apr 2002.

[35] W. Yao, R.-B. Liu, and L. J. Sham, "Theory of electron spin decoherence by interacting nuclear spins in a quantum dot," *Phys. Rev. B*, vol. 74, p. 195301, Nov 2006.

[36] B. Braunecker, P. Simon, and D. Loss, "Nuclear magnetism and electron order in interacting one-dimensional conductors," *Phys. Rev. B*, vol. 80, p. 165119, Oct 2009.

[37] C. P. Scheller, T.-M. Liu, G. Barak, A. Yacoby, L. N. Pfeiffer, K. W. West, and D. M. Zumbühl, "Possible evidence for helical nuclear spin order in gaas quantum wires," *Phys. Rev. Lett.*, vol. 112, p. 066801, Feb 2014.

[38] P. Simon and D. Loss, "Nuclear spin ferromagnetic phase transition in an interacting two dimensional electron gas," *Phys. Rev. Lett.*, vol. 98, p. 156401, Apr 2007.

[39] P. Simon, B. Braunecker, and D. Loss, "Magnetic ordering of nuclear spins in an interacting two-dimensional electron gas," *Phys. Rev. B*, vol. 77, p. 045108, Jan 2008.

[40] S. Datta, *Electronic Transport in Mesoscopic Systems*. Cambridge Studies in Semiconductor Physi, Cambridge University Press, 1997.

[41] P. Mello and N. Kumar, *Quantum Transport in Mesoscopic Systems: Complexity and Statistical Fluctuations, a Maximum-entropy Viewpoint*. Mesoscopic physics and nanotechnology, Oxford: Oxford University Press, 2004.

[42] M. Z. Hasan and C. L. Kane, "*Colloquium* : Topological insulators," *Rev. Mod. Phys.*, vol. 82, p. 3045, 2010.

[43] J. E. Moore, "The birth of topological insulators," *Nature*, vol. 464, no. 7286, p. 194, 2010.

[44] A. M. Lunde and G. Platero, "Hyperfine interactions in two-dimensional HgTe topological insulators," *Phys. Rev. B*, vol. 88, p. 115411, 2013.

[45] J. Puebla, E. Chekhovich, M. Hopkinson, P. Senellart, A. Lemaitre, M. Skolnick, and A. Tartakovskii, "Dynamic nuclear polarization in ingaas/gaas and gaas/algaas quantum dots under nonresonant ultralow-power optical excitation," *Physical Review B*, vol. 88, no. 4, p. 045306, 2013.

[46] J. Tian, S. Hong, I. Miotkowski, S. Datta, and Y. P. Chen, "Observation of current-induced, long-lived persistent spin polarization in a topological insulator: A rechargeable spin battery," *Science Advances*, vol. 3, no. 4, 2017.

[47] Y. Tanaka, A. Furusaki, and K. A. Matveev, "Conductance of a helical edge liquid coupled to a magnetic impurity," *Phys. Rev. Lett.*, vol. 106, p. 236402, Jun 2011.

[48] J. Schliemann, A. Khaetskii, and D. Loss, "Electron spin dynamics in quantum dots and related nanostructures due to hyperfine interaction with nuclei," *Journal of Physics: Condensed Matter*, vol. 15, no. 50, p. R1809, 2003.

[49] S. E. Economou and E. Barnes, "Theory of dynamic nuclear polarization and feedback in quantum dots," *Phys. Rev. B*, vol. 89, p. 165301, Apr 2014.

[50] A. Russo, E. Barnes, and S. E. Economou, "Dynamic nuclear polarization from topological insulator helical edge states," *Phys. Rev. B*, vol. 98, p. 235412, Dec 2018.

[51] A. Vezvaee, A. Russo, S. E. Economou, and E. Barnes, "Topological insulator ring with magnetic impurities," *Phys. Rev. B*, vol. 98, p. 035301, Jul 2018.

[52] A. M. Lunde and G. Platero, "Helical edge states coupled to a spin bath: Current-induced magnetization," *Phys. Rev. B*, vol. 86, p. 035112, 2012.

[53] D. McCamey, J. Van Tol, G. Morley, and C. Boehme, "Electronic spin storage in an electrically readable nuclear spin memory with a lifetime> 100 seconds," *Science*, vol. 330, no. 6011, pp. 1652–1656, 2010.

[54] A. M. Bozkurt, B. Pekerten, and I. Adagideli, "Work extraction and landauer's principle in a quantum spin hall device," *Phys. Rev. B*, vol. 97, p. 245414, Jun 2018.

[55] A. Mert Bozkurt, B. Pekerten, A. Asgharpour, and I. Adagideli (Manuscript in preparation), 2019.

Appendix A

DETAILS OF THE NUMERICAL SIMULATION

In this appendix, we explain the inner workings of our program that we use to obtain the plots of probability of total reflection. For a given number of nuclei, N, and a particular reflection amplitude, r, the program creates all possible initial nuclear spin configurations and " dynamically" builds a tree of probability for each configuration. We describe this "dynamical building" below. While creating a tree, it starts with the initial nuclear spin configuration and a spin-up electron incoming from the left, utilizing the single-interaction dynamics for the first nuclear spin. If the nuclear spin is parallel, the electron passes the nuclear spins until it finds an anti-parallel one. If the encountered nuclear spin is anti-parallel, the program saves the current nuclear configuration and the branch point to a dynamic list, and always chooses the transition path first. This process continues until the program finds an output state, which is defined by the position of the electron, as it is either at where it starts or at the further end of the nuclear region. When an output with the electron at the starting point is found, i.e., a total reflection occured, the final nuclear spin configuration and the multiplication of the single-nucleus scattering amplitudes for reflection and transition, r and t, along the path that is connecting the initial and final states, are saved to an output list. The program then jumps back to the previous branch by using the dynamic list in which the intermediate configurations and the branch points are stored, and takes the reflection path, updating the electron and nuclear spin according to the polarization. It then repeats the same process until it finds another output of total reflection. A diagram for an example of two nuclear spins is shown in Figure A.1.

After going over the entire tree, the program organizes the list of outputs: Since there exist multiple identical outputs for a given input in many cases, it sums over the paths leading to identical outputs, thus obtaining the numerical value for the inner product given in Equation 4.2. It then sums the squares of the amplitudes and proceeds to the next initial configuration. When all the initial configurations are done, the program sums and takes the average over all inputs, since the distribution of nuclear spins would be random in a realistic system. This final value is written into a .txt file. The whole process described

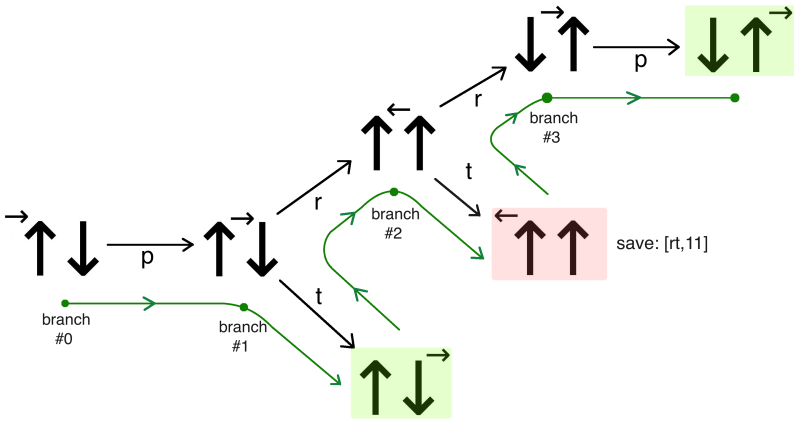

Figure A.1: The diagram of how the program works for a simple example of two nuclear spins. Vertical arrows represent the nuclear spins, while the smaller, horizontal one is for the electron. A right-going electron has an up-spin, due to spin-momentum locking. Data for the case of total reflection, highlighted in red, is saved. 11 stands for up-up.

above is repeated for the next r value, proceeding until the whole range of $0 \leq |r|^2 \leq 1$ is covered in 101 iterations. After all the iterations are done, we use the data recorded in the .txt file to obtain our plots shown in figures 4.2 and 4.3. For the plots of individual initial nuclear configurations shown in Figure 4.4, the same procedure applies, this time for the desired input state only, without any averaging.